FOREIGN
BROADCAST
INFORMATION
SERVICE

JPRS Report

Science & Technology

China

19980506 051

DTIC QUALITY INSPECTED 8

Science & Technology
China

CONTENTS

AEROSPACE

ADVANCED MATERIALS

BIOTECHNOLOGY

COMPUTERS

LASERS, SENSORS, OPTICS

TELECOMMUNICATIONS R&D

PHYSICS

Development of Liquid Propellant Engines for the Long March Family of Launch Vehicles

90FE0339A Beijing YUHANG XUEBAO [JOURNAL OF CHINESE SOCIETY OF ASTRONAUTICS] in Chinese No 3, 31 Jul 90 pp 5-9

[Article by Zhu Ningchang [2612 1380 2490] of the 11th Institute, Ministry of Aeronautics and Astronautics]

[Text]

I. Introduction

Since the Soviet Union launched the first artificial earth satellite on 4 October 1957, astonishing progress has been made in aerospace technology. During the past three decades, more than 3,000 spacecraft designed for various applications have been launched; these satellites have made major contributions in the areas of communications, meteorology, navigation, defense, and scientific research. Progress in aerospace technology has become an important measure of a nation's overall scientific achievement.

Liquid propellant engines are widely used on launch vehicles and space systems because of their superior performance, flexibility, economy and reliability. In the foreseeable future, it is expected that the development of aerospace technology will depend on the ability to develop state-of-the-art propulsion technology for liquid propellant rockets.

To meet the needs of the rapidly growing aerospace industry, it is necessary to establish a long-term plan for developing liquid-propellant rocket engines. In this article, an attempt is made to analyze the future development trend of liquid-propellant propulsion technology based on the requirements imposed by the advancing aerospace technology and the current status of liquid propulsion of the Long March family of launch vehicles. The discussion will cover various liquid propellant rocket engines with applications for launch vehicles and spacecraft.

II. Liquid Propellant Propulsion System for the Long March Family of Launch Vehicles

Since the launch of the "Dong Fang Hong-1" satellite by the "Long March-1" (CZ-1) launch vehicle on 24 April 1970, significant progress had been made in China's

aerospace technology. The successful launches of scientific experimental satellites, retrievable remote sensing satellites and geosynchronous communications satellites attracted world-wide attention. China's "Long March-2" (CZ-2) and "Long March-3" (CZ-3) launch vehicles have entered the international market for launching and carrying foreign satellites. On 7 September 1988, the "Feng Yun-1" sunsynchronous meteorological satellite was successfully launched by China's newly developed "Long March-4" (CZ-4) launch vehicle.

The "Long March-1" is a three-stage rocket; the first two stages use the liquid propellant—red smoke nitric acid/UDH [unsymmetrical/dimethyl/hydrazine], and the third stage is a solid propellant rocket. The rocket has a lift-off weight of 81.6 tons and a lift-off thrust of 1098 k-N; it has a diameter of 2.25 m and a total length of 29.45 m. It is capable of launching a 300-kg scientific experiment satellite into near-earth orbit. The first-stage propulsion system consists of 4 independent engines. The second-stage engine uses a fiberglass extension to increase the nozzle area ratio, and is cooled by turbine waste gas.

The "Long March-2" is a two-stage rocket which uses nitrogen tetroxide/UDH as propellant. It has a lift-off weight of 191 tons, a diameter of 3.35 m and a length of 31.65 m. It is capable of carrying a 2,000 kg payload into near-earth orbit, and has successfully launched a number of retrievable remote-sensing satellites; it has also carried out launch missions for France and the Federal Republic of Germany. The first-stage propulsion system consists of 4 engines; each engine can swivel plus or minus 10° to provide attitude control torque. The second-stage consists of a main engine and 4 floating engines which can swivel plus or minus 60° in the tangential direction for attitude control.

The "Long March-3" and "Long March-4" are both three-stage liquid propellant rockets; the first and second stages use storable propellants. The third stage of the "Long March-3" uses liquid oxygen/liquid hydrogen propellant and has been used for launching a number of geosynchronous communications satellites. The "Long March-4" has a lift-off thrust of 2,942 k-N; its third stage has two storable-propellant engines and has been used for launching sunsynchronous meteorological satellites.

The key performance parameters for the liquid propulsion systems of the Long March family of launch vehicles are given in Table 1.

Table 1. Key Performance Parameters for the Liquid Propulsion System of the Long March Launch Vehicles

Model Number		Propellant	Mix Ratio	Thrust (kN)	Specific Impulse (m/s)	Combustion Chamber Pressure (MPa)
CZ-1	First stage	Red-smoke nitric acid/UDH	2.46	1098	2363	6.57
	Second stage	Red-smoke nitric acid/UDH	2.48	320	2814	6.31

Table 1. Key Performance Parameters for the Liquid Propulsion System of the Long March Launch Vehicles (Continued)

Model Number		Propellant	Mix Ratio	Thrust (kN)	Specific Impulse (m/s)	Combustion Chamber Pressure (MPa)
CZ-2	First stage	Nitrogen tetroxide/ UDH	2.10	2785	2540	6.98
	Second stage main engine, floating engines	Nitrogen tetroxide/ UDH	2.18	720	2835	6.52
			1.57	46.1	2762	3.29
CZ-3	First stage	Nitrogen tetroxide/ UDH	2.10	2785	2540	6.98
	Second stage main engine, floating engines	Nitrogen tetroxide/ UDH	2.18	720	2835	6.52
			1.57	46.1	2762	3.29
	Third stage	Liquid oxygen/liquid hydrogen	5.0	44.1	4168	2.63
CZ-4	First stage	Nitrogen tetroxide/ UDH	2.12	2942	2550	7.44
	Second stage main engine, floating engines	Nitrogen tetroxide/ UDH	2.18	720	2835	6.52
			1.57	46.1	2762	3.29
	Third stage	Nitrogen tetroxide/ UDH	2.15	98	2942	4.41

Note: (1) The third stage of CZ-1 is a solid-propellant rocket. (2) The second stage of CZ-2, -3, -4 consists of a main engine and floating engines.

III. Development Trend of Liquid-Propellant Rocket Engines

In order to satisfy the future needs of aerospace technology in terms of launching large applications satellites, manned space stations or space planes, it is necessary to develop not only large launch vehicles but also orbit maneuver systems, orbit transfer systems and auxiliary propulsion systems. The following analysis of the development trend of various types of liquid-propellant rocket engines is based on their potential applications in launch vehicles and spacecraft.

1. Large Liquid-Propellant Booster Engines

In order to meet the needs of future aerospace development, the payload capability of launch vehicles must be enhanced. This can be accomplished by taking the following design approaches:

1) strap solid or liquid propellant booster rockets to the main engine;

2) develop large liquid-propellant booster engines;

3) develop high-performance liquid oxygen/liquid hydrogen engines;

4) increase propellant volume and extend engine burn time;

5) increase the dimensions of the satellite fairing.

The modified design of the "Long March-2," the "Long March-2E" (CZ-2E), plans to use liquid-propellant boosters to increase the lift-off thrust to 5,884 k-N. The specific impulses of the second-stage main engine and floating engine are increased from 2,835 m/s and 2,762 m/s to 2,903 m/s and 2,835 m/s respectively by increasing the nozzle area ratio. The "Long March-2E" is designed to launch large applications satellites for Australia and the United States.

Another design approach that should be considered is to develop new, high-capacity launch vehicles and associated propulsion systems. In particular, development of low-cost, pollution-free, high-performance and reusable liquid-propulsion systems should be considered for launching manned space stations, space planes and large spacecraft.

An important consideration in the design of large liquid booster engine is to select the appropriate propellant. Currently, three types of propellants can be selected: (1) liquid oxygen/liquid hydrogen; (2) liquid oxygen/hydrocarbon; and (3) storable propellant. Liquid oxygen/liquid hydrogen has very high specific impulse, but the low density of liquid hydrogen requires a large rocket structure. Liquid oxygen/hydrocarbon is clearly superior to storable propellants in terms of performance, cost, low pollution level, absence of corrosion, and reusability.

It should be pointed out that a high-performance, large liquid oxygen/hydrocarbon booster engine design

requires a high combustion chamber pressure. Therefore, special attention must be given to the physical and chemical properties of hydrocarbon fuels such as ignition characteristics, combustion efficiency and stability, cooling characteristics, carbon accumulation in the combustion chamber, coke formation in the regenerative cooling system, and compatibility with surrounding materials. Study has shown that it is feasible to use liquid-hydrocarbon as propellant for the booster engines of large launch vehicles. The engine design should be based on the technical requirements, and the choice of a specific hydrocarbon fuel such as methane, propane, or kerosene is determined by the chamber pressure. The study has also considered a fuel in which a small amount of liquid hydrogen is added to liquid oxygen and hydrocarbon.

2. Liquid Oxygen/Liquid Hydrogen Engines

Liquid oxygen/liquid hydrogen has become a widely used propellant because of its high specific impulse and clean exhaust; it is often used as propellant for the second-stage main engine and upper stage engines.

However, the low density and high volatility of liquid hydrogen requires heavy insulation; as a result, the dimensions of the launch vehicle must be increased. In order to take full advantage of this propellant, the engine performance must be improved and its size and weight must be reduced. Generally, this can be accomplished by increasing the chamber pressure and nozzle area ratio, using a closed circulating system (e.g., supplementary combustion and vaporization circulation) and increasing the engine thrust level.

The third stage of the "Long March-3" is a liquid oxygen/liquid hydrogen engine with a thrust of 44.1 k-N and a specific impulse of 4,168 m/s; it also has double-starting capability. The reliability of this engine has been demonstrated by many successful launches of geosynchronous communications satellites. The new liquid oxygen/liquid hydrogen engine currently under development has a thrust of approximately 78.5 k-N and a specific impulse of approximately 4,315 m/s. By using two of these engines as the third stage of the modified "Long March-3," the "Long March-3A" (CZ-3A), it is possible to almost double the payload capability. It can be expected that the ever increasing demands of aerospace technology will continue to promote the use of large thrust, high performance liquid hydrogen engines.

3. Orbit Maneuver Engines and Upper Stage Engines Which Use Storable Propellants

In order to accommodate different types of launch missions such as launching high-altitude satellites and inter-planetary probes, a combination of different types of upper stage engines and booster rockets can be used. Because of the high density and low volatility of storable propellants, they are suited for long-duration space missions lasting several months or several years.

Space plane engines, which are primarily used for orbit injection corrections, orbit maneuvers and rendezvous, and de-orbit maneuvers, generally use storable propellants and compression type supply systems. An orbit maneuver engine should have multiple starting and thrust adjustment capabilities; it must also be able to operate reliably in a high-vacuum, high radiation, and weightless environment.

The third stage of the "Long March-4" launch vehicle uses a pump-compression type upper-stage engine with storable propellants; it has double-starting and bi-directional swivel capability, and its specific impulse is greater than 2,942 m/s.

The performance of the space plane engine can be improved by designing high-performance injectors and large area ratio nozzles.

4. Auxiliary Propulsion Systems

The auxiliary propulsion system is an important component of space launch systems and spacecraft; it has become an important branch of liquid propellant rocket propulsion technology. The primary functions of an auxiliary propulsion system include attitude control, velocity correction, orbit transfer and correction, position keeping, and providing auxiliary power on a spacecraft. This type of propulsion system must be able to start reliably under vacuum and weightless conditions; it must be capable of either continuous or pulse operation, with the total number of starts as high as several hundred thousand times.

Most auxiliary propulsion systems use single-constituent or double-constituent liquid propellant engines; gas-jet propulsion is used only in cases where the total impulse requirement is very small.

The single-constituent hydrazine catalytic decomposition engine has many advantages including simple structure, responsiveness, stability, and good repeatability in pulse operation; it has been widely used for attitude control, normal thrusting, terminal velocity correction, propellant precipitation and position keeping of various spacecraft and launch systems.

The single-constituent hydrazine gas generator can be used to drive the turbine of an auxiliary power unit of a space plane; the turbine in turn drives a hydraulic pump or an electric motor for controlling the rudders, landing gears and brakes, the separation of external storage tanks and the swivel of solid booster nozzles. In addition, it can be used as the emergency power supply of the space plane.

In the mid 1960's, China had started developing a single-constituent hydrazine catalytic decomposition engine for attitude control of the upper stage of launch vehicles and spacecraft. It has now developed into a family of single-constituent engines with thrust levels ranging from 5.5 to 1,000 k-N and specific impulses ranging from 2,059 to 2,206 m/s.

Because of the relatively high freezing point (1.4°C) of hydrazine, electric heaters are required to keep it from freezing in a cold environment; this would impose increased structural weight and complexity in the design. For this reason, studies were initiated in the early 1970's to develop low-freezing-point single-constituent propellants. Currently, the "Dan Tui-3" propellant with a freezing point of -30°C has been successfully tested on the ground and in flight; the test results show that the "Dan Tui-3" has good vacuum ignition and cold-start characteristics, and its specific impulse is 20 m/s higher than that of hydrazine. With the feasibility of "Dan Tui-3" demonstrated in auxiliary propulsion systems, efforts are under way to develop a family of "Dan Tui-3" attitude control engines with different specifications; the thrust levels of these engines range from 24.5 to 1,000 N.

To meet the increasingly higher demands on total specific impulse and performance of auxiliary propulsion systems, attitude control engines using double-constituent propellants have also been developed. In the early 1970's, China began developing such engines using nitro-oxide and hydrazine fuels with thrust levels ranging from 19.6 to 1,520 N. With the exception of one design which used a pump compression system, the other designs all used constant-pressure or decreasing-pressure compression systems. These engines included a 490-N apogee engine and variable-thrust engines. Liquid-propellant apogee engines have a number of advantages over solid-propellant engines: low thrust level, small impulse deviation, multiple starting capability and high orbit injection accuracy.

The nitrogen tetroxide/mono-methyl hydrazine combination has many desirable properties including wider temperature range in its liquid state, good high-altitude ignition characteristics, low pollution level, high performance and combustion stability; as a result, it is widely used in various spacecraft engines and in unified auxiliary propulsion systems which combine apogee engine with attitude control engine.

In addition, there is also a single-constituent and double-constituent design where the double-constituent propellant nitrogen tetroxide/hydrazine is used for the apogee engine and the single-constituent propellant hydrazine is used for attitude control and position keeping.

It should be pointed out that liquid oxygen/hydrocarbon auxiliary propulsion systems are also under development and are expected to be used in the future.

IV. Conclusions

1) In order to satisfy the future development needs of aerospace technology, it is necessary to establish a long-term plan for developing liquid propulsion technology and for systematically improving the performance of liquid-propellant rocket engines.

2) The long-term development plan should include the following items:

a. large liquid oxygen/hydrocarbon booster engines;

b. high-performance liquid oxygen/liquid hydrogen engines;

c. storable-propellant orbit maneuver engines and upper-stage engines;

d. single-constituent (hydrazine, Dan Tui-3) and double-constituent attitude control engines.

3) Extensive research efforts should be devoted to key technology areas and the required research facilities should be established.

New Mechanism for Solid Propellant Ignition

[Article by Zhang Jiaxin [1728 0163 1800] of the Harbin Institute of Ship Engineering, Space Engineering Dept.]

[Text]

I. Introduction

In the study of solid propellant ignition, several theoretical models have been proposed in the literature.[1] Most of the models assume that any condensed phase substance in the igniter has evaporated before ignition takes place; this assumption is clearly unrealistic when the ignition agent contains condensed phase particles.[2] If the ignition agent contains magnesium or aluminum powders, the oxides of these substances in the 3,000°K hot gas will be in a liquefied state. When these particles are in contact with the propellant surface, the rate of heat exchange with the propellant will be significantly increased, thereby reducing the ignition time. Research in this area is rather limited at the present time; in Ref. [3], some results of experimental research and theoretical analysis with numerical solutions can be found. In this paper, a new hypothesis of the ignition mechanism of flowing hot gas containing condensed phase substances is proposed; the proposed mechanism is based on the experimental evidence that if the ignition time is short and the propellant surface fails to reach ignition temperature, a layer of deposition substance will be formed over the surface. A theoretical model based on this mechanism has been developed for the ignition process of flowing hot gas containing condensed phase substance; this model can be used to determine the time variation of internal temperature distribution, surface temperature, and the thickness of the condensed layer. In addition, an analytical solution of the ignition time delay is obtained, and a numerical example is presented. Also, based on the theory of convective heat transfer, the relationship between ignition time delay and pressure is derived; it is shown that the results of theoretical analysis compare favorably with the experimental results of Ref. [4]. To test the validity of the proposed mechanism of

ignition deposition, an experiment has also been conducted. While the experiment did not provide any quantitative results at this time, it has verified the occurrence of the deposition process prior to ignition, and has also shown that the deposition layer can be of considerable thickness.

II. Experiment

The main objective of this experiment is only to provide a qualitative description of the deposition mechanism during the ignition process; it is not intended to provide quantitative measurements, for which additional in-depth experimental research would be required.

The experimental setup is shown in Figure 1, where the ignition charge (30% Al powder, 70% NH_4ClO_4) is placed inside a miniature engine whose interior dimensions are: 6mm in diameter and 22mm in length, and whose nozzle diameter is 2mm. The engine is rigidly attached to a support frame, and a small block of poly-sulphur propellant (20mm x 20mm, 5mm thick) is positioned in front of the engine nozzle; the propellant block is completely covered except for one side. Between the engine nozzle and the propellant block is a rotating disk with a small opening. When the disk rotates to a position where the opening is aligned with the engine nozzle, the igniting hot gas flows through the opening and over the surface of the propellant block. Thus, by varying the width of the opening and the rotational speed of the disk, it is possible to control the heating time of the propellant block so that ignition does not occur. The results of this experiment show that as long as the propellant is not ignited, a deposition layer will form on the propellant surface. Figure 2 shows a comparison of two photographs taken under a microscope of the propellant block with and without the deposition layer; the photograph clearly shows the deposition of Al_2O_3 particles.

Miniature
ignition device

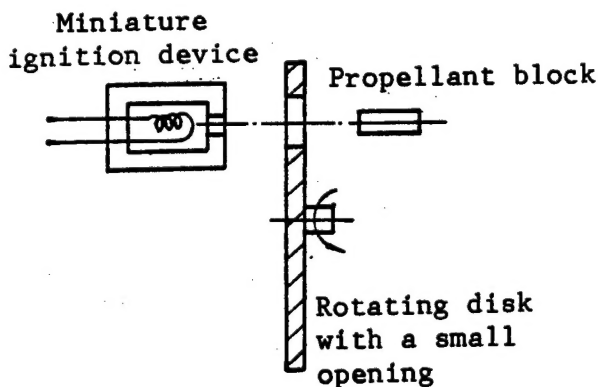Propellant block

Rotating disk
with a small
opening

Figure 1. Schematic Diagram of the Experimental Setup

Figure 2. Microscopic Photographs of the Propellant Surface With and Without Deposition (magnified 60 times)

III. Theoretical Model

At $t \leq 0$, the propellant and the surrounding air are both at ambient temperature T_0; at $t = 0$, heat transfer between the condensed phase hot particles and the propellant begins to take place. The gas phase process of the hot gas flowing over the deposition surface can be treated by considering the coefficient of heat transfer h; the temperature distribution of the ignition model is shown in Figure 3.
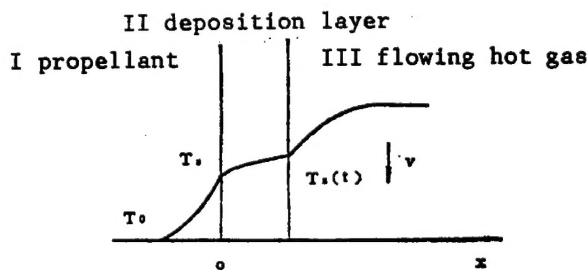

Figure 3. Surface Deposition Ignition Model

The approach is to derive a set of differential equations based on the model and to obtain an analytical solution of the equations. The boundary condition $T_s(t)$ is assumed to be equal to the surface temperature of the solid phase as determined by the flowing hot gas model, T_s. This assumption is justified because during the initial stage of ignition, the deposition layer is very thin; also since

$$\lambda_1 \frac{\partial T_1}{\partial x}\bigg|_{x=0} = \lambda_2 \frac{\partial T_2}{\partial x}\bigg|_{x=0}$$

and $gl_1 \ll \lambda_2$, the slope of the temperature gradient in region I is much greater than the slope in region II, i.e., the temperature variation in region II is very small.

In Ref. [1], the ignition model of the flowing hot gas is used to obtain the expression:

$$T_s = T_0 + (T_g - T_0)[1 - e^{\frac{h^2}{\lambda_1^2} a_1 t} \mathrm{erfc}(h\sqrt{a_1 t}/\lambda_1)]$$

where the subscript 1 denotes the propellant, the thermal diffusion coefficient $a_1 = \lambda_1/\rho_1 C_{p1}$, and the complementary error function is defined by .

$$\mathrm{erfc}(Z) = \frac{2}{\sqrt{\pi}} \int_z^{\infty} e^{-x^2} dx$$

In order to establish a mathematical model for ignition of the propellant by the condensed substance after combustion of the ignition charge, we propose the following assumptions:

1. The hot gas flow is one-dimensional and non-stationary.

2. All chemical reactions of the solid phase and gas phase are neglected.

3. The ignition hot gas contains condensed particles in either liquid or solid state; the size of the particles is of the order of microns.

4. The heat released by the collision of the hot particles on the propellant surface is considered to have the effect of only increasing the convective heat transfer coefficient.

5. As soon as the hot particles are deposited on the propellant surface, heat transfer begins to take place, and it continues until the two temperatures are equalized.

6. The physical parameters of the propellant and the hot particles (Al_2O_3), i.e., the density ρ and the constant-pressure specific heat C_p, are both constants.

7. $T_s(t) = T_s$.

Control equations:

$$\frac{\partial T_1}{\partial t} = a_1 \frac{\partial^2 T_1}{\partial x^2}, \quad \frac{\partial T_2}{\partial t} = a_2 \frac{\partial^2 T_2}{\partial x_2}.$$

(the subscripts 1 and 2 denote conditions in the propellant and in the condensed layer respectively)

Boundary conditions:

$$T_1|_{x=-\infty} = T_0, \quad T_2|_{x=\infty} = T_s(t)$$

Initial conditions:

$$T_1|_{t=0} = T_0, \quad T_2|_{t=0} = T_0$$

Energy conservation equation at x = 0:

$$\lambda_1 \frac{\partial T_1}{\partial x}\bigg|_{x=0} = \lambda_2 \frac{\partial T_2}{\partial x}\bigg|_{x=0}$$

Condition of temperature continuity:

$$T_1|_{x=0} = T_2|_{x=1}$$

By applying the method of Laplace transform,[5] a solution of the control equations which satisfies the initial and boundary conditions can be obtained:

$$T = T_0 + \frac{T_g - T_0}{1 + \frac{\lambda_1}{\lambda_2}\sqrt{\frac{a_1}{a_2}}}\left[-e^{\frac{h^2}{\lambda_1^2}a_1 t - \frac{h}{\lambda_1}x} \, \mathrm{erfc}\left(\frac{h}{\lambda_1}\sqrt{a_1 t} - \frac{x}{2\sqrt{a_1 t}}\right) \right.$$

$$\left. + \mathrm{erfc}\left(\frac{-x}{2\sqrt{a_1 t}}\right)\right] \qquad (x < 0)$$

$$T_2 = T_0 + (T_g - T_0)\left[1 - e^{\frac{h^2}{\lambda_1^2}a_1 t}\,\mathrm{erfc}\left(\frac{h}{\lambda_1}\sqrt{a_1 t}\right)\right] + \frac{T_g - T_0}{1 + \frac{\lambda_2}{\lambda_1}\sqrt{\frac{a_1}{a_2}}}$$

$$\cdot\left[e^{\frac{h}{\lambda_1}\sqrt{\frac{a_1}{a_2}}x + \frac{h^2}{\lambda_1^2}a_1 t}\,\mathrm{erfc}\left(\frac{h}{\lambda_1}\sqrt{a_1 t} + \frac{x}{2\sqrt{a_2 t}}\right) - \mathrm{erfc}\left(\frac{x}{2\sqrt{a_2 t}}\right)\right] \quad (x > 0)$$

At x = 0,

$$T_s = T_{1(0)} = T_{2(0)} = T_0 + \frac{T_g - T_0}{1 + \frac{\lambda_1}{\lambda_2}\sqrt{\frac{a_2}{a_1}}}\left[1 - e^{\frac{h^2}{\lambda_1^2}a_1 t}\,\mathrm{erfc}\left(\frac{h}{\lambda_1}\sqrt{a_1 t}\right)\right]$$

IV. Numerical Example

In order to verify the analytical results and to generate the temperature distribution curve and other curves of the ignition process, a numerical example is presented for a selected set of parameters. Due to the lack of transient dynamic data, the chemical and dynamic parameters used in this example are approximated by the values under steady-state combustion conditions, as shown in the following table:

Physical Parameter	Notation	Selected Value
initial propellant temperature	T_0	300°K
gas temperature	T_g	3,000°K
propellant density	ρ_1	1.7×10^3 kg/M^3
Al$_2$O$_3$ density	ρ_2	3.96×10^3 kg/M^3
propellant heat conductivity	λ_1	0.375 J/SxMxK
Al$_2$O$_3$ heat conductivity	λ_2	2.6 J/SxMxK
propellant specific heat	C_{p1}	1.2925×10^3 J/kgxK
Al$_2$O$_3$ specific heat	C_{p2}	1.730×10^3 J/kgxK
propellant thermal diffusion coefficient	α_1	1.7067×10^{-7} M^2/s
Al$_2$O$_3$ thermal diffusion coefficient	α_2	3.80×10^{-7} M^2/s
heat transfer coefficient	h	0.2×10^3 J/sxM^{2}xK

The ignition process may be defined by different criteria; for example:

1. The ignition time must be greater than some minimum ignition time $t > t_{ig}$.

2. The ignition temperature must be greater than some minimum temperature $T > T_{ig}$.

3. The ignition energy must be greater than some minimum energy $E > E_{ig}$.

In this paper, criterion No. 2 is selected, and T_{ig} is chosen to be the propellant surface temperature under steady-state combustion conditions. For a double-base charge, $T_{ig} = 1,000°K$; for a composite charge, $T_{ig} = 630°K$.

Calculated Results

From the data of this numerical example, the following results are presented.

1. Temperature distribution in the solid phase region (propellant and deposition layer), as shown in Figure 4. The figure shows good agreement between the measured temperature distribution and the theoretical result; the ignition time delay is $t_{ig} = 4$ ms, and the thickness of the deposition layer is $\delta = 90$ μm, which is consistent with the result given in the reference.

2. Time variations of the propellant surface temperature and the thickness of the deposition layer, as shown in Figure 5. The curves indicate that both the propellant surface temperature and the thickness of the deposition layer increase with time; this is consistent with actual observations.

3. Ignition time delay as a function of pressure. As shown in Figure 6, the calculated result compares favorably with the experimental result of Ref. [4].
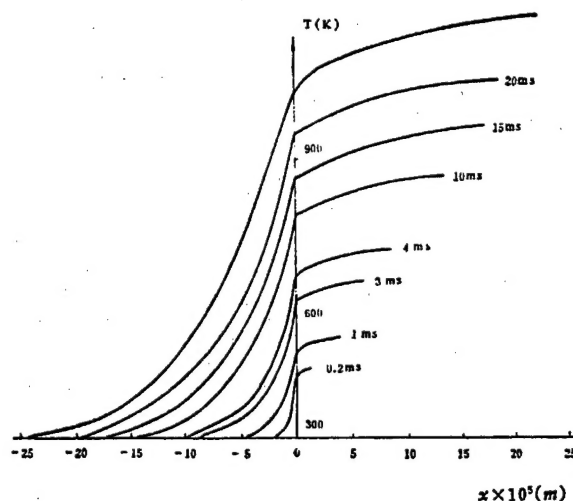

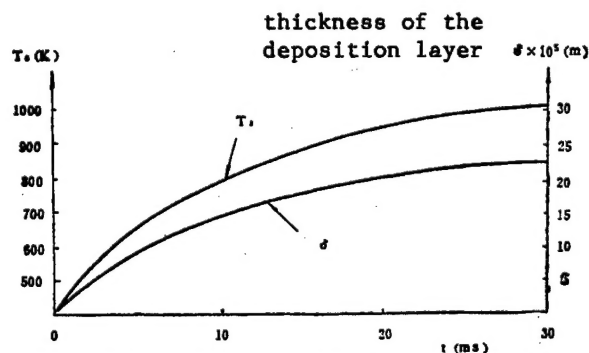Figure 4. Temperature Distribution in the Propellant and the Deposition Layer

Figure 5. Time Variation of the Propellant Surface Temperature and the Thickness of the Deposition Layer

V. Conclusions and Discussion

By comparing the results of theoretical analysis and the experimental results given in the literature, the following conclusions can be drawn:

1. The proposed condensed-particle flowing hot gas ignition model for the solid propellant is a reasonable one, and the use of numerical method to analyze the ignition process is feasible and reliable.
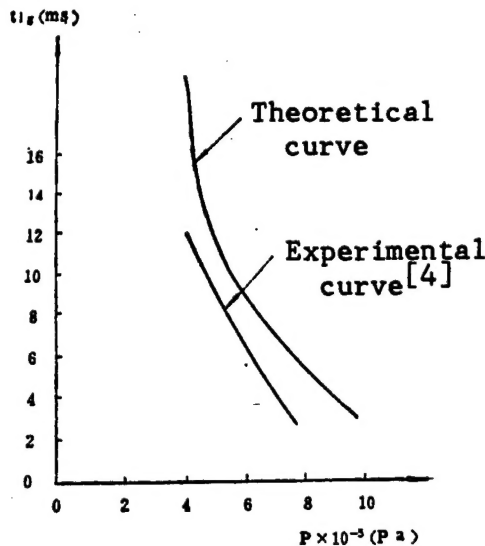
Figure 6. Comparison of Calculated Ignition Time Delay with Experiment

2. The numerical results indicate that:a. the ignition time delay decreases with increasing pressure;

b. the thickness of the deposition layer increases with time.

3. The results also pointed out that in the pressure range of 3-8 atm, the predicted ignition time delay is in close agreement with experimental measurements; this provides valuable information for studying ignition time delays in the ignition process.

4. Since the chemical and dynamic parameters used in this numerical example are based on steady-state combustion conditions, they differ from the transient state values during the ignition process. Therefore, the calculated ignition time delay and the thickness of the deposition layer also differ from their actual values, but the differences are small. The parameter which has a significant effect on the result is the convective heat transfer coefficient h. In this paper, the selected value of h, which is based on the Bartz formula, has been verified by the calculated results.

References

1. Li Fengchun, "Theory of Ignition of Solid Rocket Propellants," Technical Exchange Conference on Solid Rocket Engines (1984) Qing Dao.

2. F. A. Williams, translated by Jing Guqun, "Fundamental Problems of Solid Rocket Engines" (1979).

3. Yi Jianwen, Wang Liang, Wang Kexiu, "Effect of Solid Particles on the Ignition Properties of Composite Propellant in High Energy Charges," Technical Exchange Conference on Solid Rocket Propulsion (1985) Shao Xing.

4. Mao Genwang, "Gas Phase Ignition Model of AP Composite Propellants," Technical Exchange Conference on Solid Rocket Engines (1984) Qing Dao.

5. Gao Ye, Zhang Jiaxin, "Analytical Solution of the Time Variation of Al_2O_3 Deposition Layer Thickness Based on Heat Transfer Theory," Propulsion Technology, No. 2, 1988.

Numerical Study of Projectile Penetration

[Article by Liu Xiaoping [0491 1420 5393 of the CAS Institute of Mechanics, Xie Chunsheng [6200 2504 3932] of the Xian Modern Chemical Institute, Qin Mengzhao [4440 1322 0340] of the CAS Computational Center, and Lu Deye [0712 1795 2814] of the 52nd Institute, Armaments Ministry: "Numerical Study of Projectile Penetration Mechanism"]

[Text]

I. Introduction

The study of the mechanism of projectile penetration is a study of the interaction between a high-speed projectile (900-1500 m/s) and a target when they collide with one another. It is a very complicated problem because it depends on many factors including the projectile velocity, the projectile diameter, the projectile shape (the nose shape and the slender ratio), the projectile material, the target material and the target thickness. For such problems, measurement techniques can only capture the exterior of the projectile and the target during the collision process. An effective approach for studying the detailed mechanism of penetration would be through numerical methods.

In this article, numerical calculations using the CPG-LTDL code[5] and an elasto-plastic fluid mechanical model[1] are presented for three different test conditions: a tungsten projectile colliding with a steel target at 1000 m/s, a steel projectile colliding with a steel target at 1000 m/s, and a steel projectile colliding with an aluminum target at 1000 m/s. The calculated results are analyzed and compared with experimental data.

II. Basic Equations

The following forms of constitutive relation and state equation are used in the two-dimensional non-steady elasto-plastic fluid mechanical equations.

1. Constitutive Relation

$$\dot{S}_{ij} = 2G\dot{\varepsilon}_{ij} + \omega_{ij}$$

where G is the modulus of rigidity, whose value is given in Table 1.[3] ω_{ij} is the correction term for rotation.

Table 1

Material	Fe	Al	W
G (10^{11} Pa)	0.81	0.274	0.144

2. von Mises Yield Criterion

$$S_{ij} \cdot S_{ij} = \frac{2}{3} Y^2$$

3. Strength Equation

$$\begin{cases} Y = Y_0 \left(1 - \frac{I}{I_m}\right) & \text{当 } I < I_m \\ Y = 0 & I \geq I_m \end{cases}$$

where Y_0 is the dynamic strength of the material under normal temperature and pressure conditions, and I_m is the melting specific internal energy of the material whose values are given in Table 2.

Table 2

	Steel Projectile	Steel Target	Aluminum Target	Tungsten Projectile
Y_0 (10^9 Pa)	0.74	0.38	0.489	0.85
I_m (J/kg)	1.30×10^6	1.30×10^6	7.0×10^5	2.28×10^5

4. State Equation

(1) $p = A_1\mu + A_2\mu^2 + A_3\mu^3 + B_1\mu I$

where

$$\mu = \frac{\rho}{\rho_0} - 1$$

This equation is used in the calculations for the cases of a steel projectile colliding with a steel target or with an aluminum target; the coefficients of this equation are given in Table 3.[2]

Table 3

Material	A_1 (10^{11} Pa)	A_2 (10^{11} Pa)	A_3 (10^{11} Pa)	B_1 (10^3 kg/m^3)	ρ_0 (10^3 kg/m^3)
Fe	1.236	2.452	5.139	17.16	7.85
Al	0.765	1.659	3.428	5.44	2.79

(2) Tillotson State Equation

This equation is used in the calculation for the case of a tungsten projectile colliding with a steel target; the parameters of the materials are taken from Ref. [3].

5. Destruction Criterion

The destruction criterion is based on the specific volume; i.e., the material is destroyed when the relative specific volume V/V_0 reaches a certain value. The values used in this paper are given in Table 4.[3]

Table 4

	Fe	Al	W
V/V_0	1.03	1.015	1.052
ρ/ρ_0	0.97	0.985	0.95

III. Initial and Boundary Conditions and the Distribution of Finite Difference Grid

1. Tungsten Projectile Colliding with a Steel Target (W→Fe)

The initial conditions are:

	Material	Y_0 (10^9 Pa)	Density ρ_0 (10^3 kg/m^3)	z-velocity v(m/s)	r-velocity u(m/s)	Specific Internal Energy l_c (J/kg)	Projectile Length (or Target Thickness)	Projectile or Target Diameter
Tungsten projectile	W-alloy	0.85	18.0	1000	0	6.36943	40 mm	4 mm
Steel target	A3	0.38	7.85	0	0	3.88888	20 mm	80 mm

The boundary conditions are (see Figure 1):

GC - the pressure and velocity are continuous at the interface between the projectile and the target

FA - on the axis of symmetry, u = 0 and the shear stress τ = 0.

All other boundaries are free with p = 0, τ = 0.

The grid spacings in both r and z directions are non-uniform; if I,J denote the grid coordinates, then the grid spacings are as follows:

I				1 → 4				5 → 24			25 → 49		
Δr (mm)				0.5				0.75			1.0		
J	1 → 7	8 → 12	13	14	15	16	17	18	19	20	21	22	23 → 100
Δz (mm)	1.5	1.4	1.3	1.2	1.1	1.0	0.9	0.8	0.75	0.70	0.65	0.60	0.50

2. Steel Projectile Colliding with a Steel Target (Fe → Fe)

The initial conditions are:

	Material	Y_0 (10^9 Pa)	v (m/s)	u (m/s)	l_0 (J/kg)	Projectile Length (or Target Thickness)	Projectile or Target Diameter	ρ_0 (10^3 kg/m3)
Steel projectile	45 # steel	0.74	1000	0	0	30 mm	12.7 mm	7.85
Steel target	A3 steel	0.38	0	0	0	20 mm	80 mm	7.85

The boundary conditions are (see Figure 2):

Fa - on the axis of symmetry, u = 0, τ = 0.

GC - at the interface of the projectile and the target, pressure and velocity are continuous.

All other boundaries are free with p = 0, τ = 0.

The grid spacing in the r direction is non-uniform:

I	1 → 5	6 → 35	36	37 → 49
Δr (mm)	1.05	1.10	1.75	1.00

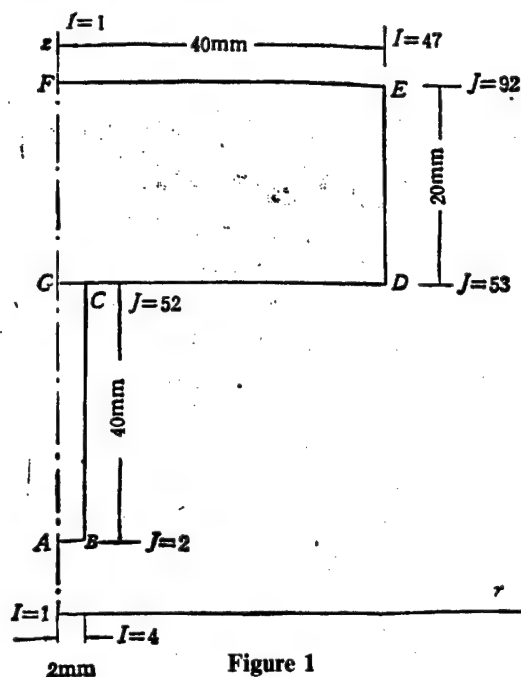The grid spacing in the z-direction is uniform: $J = 1 \to 100$, $\Delta z = 1$ mm.

Figure 1
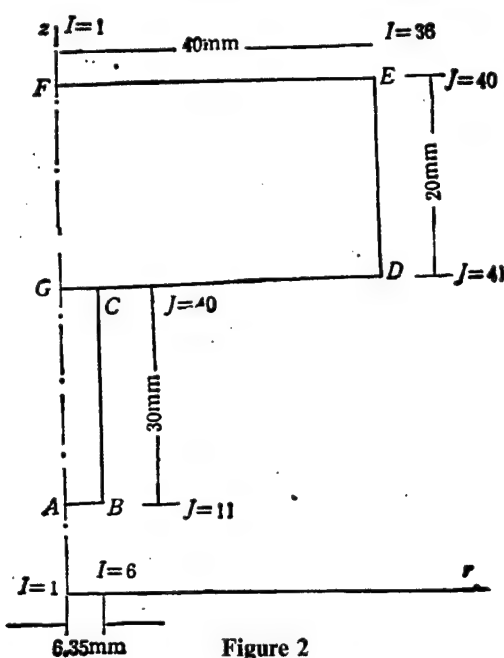

Figure 2

3. Steel Projectile Colliding With an Aluminum Target (Fe → Al)

The boundary conditions and grid spacings are the same as for the Fe → Fe case; the initial conditions are:

	Material	Y_0 (10^9 Pa)	v (m/s)	u (m/s)	I_0 (J/kg)	ρ_0 (10^3 kg/ m³)	Projectile Length (or Target Thickness)	Projectile or Target Diameter
Steel projectile	45 # steel	0.74	1000	0	0	7.85	30 mm	12.7 mm
Aluminum target	LY12	0.489	0	0	0	2.79	20 mm	80 mm

IV. Comparison of Calculated and Experimental Results

1. The Projectile and Target Configuration During the Penetration Process

The calculated results for the case of W → Fe at 1000 m/s show that the diameter of the penetration hole is essentially uniform, and is approximately equal to twice the projectile diameter. By comparing the calculated projectile-target configuration with the high-speed photographs of a test projectile at 1012 m/s, it is possible to determine the relative positions of the projectile and the target at different times (Table 5) and the entrance and exit dimensions of the penetration hole at three different projectile velocities (Table 6).
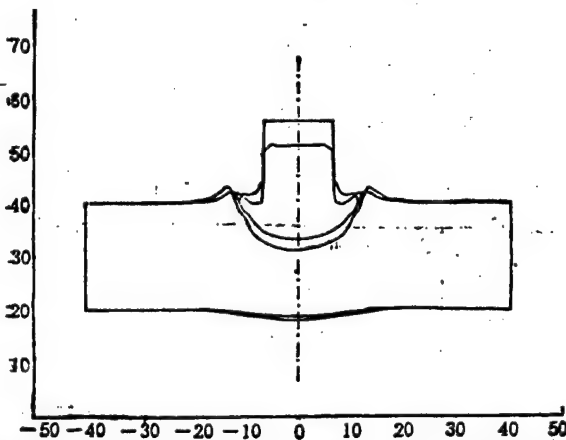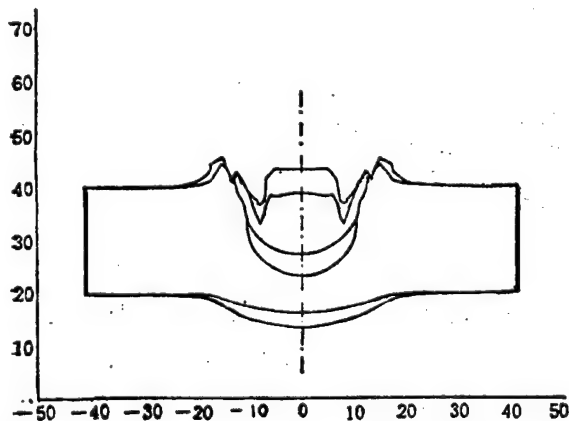
Table 5. Relative Positions of the Projectile and the Target at Different Times

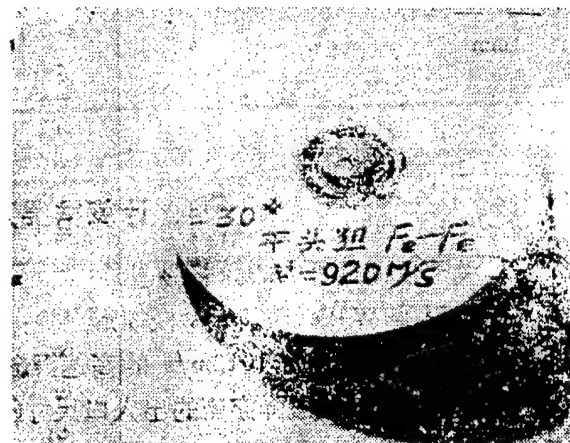|	Test Result	Calculated Result	Test Result	Calculated Result	Test Result	Calculated Result	Test Result	Calculated Result
t (µs)	9.25	10.0	20.35	20.0	29.6	30.0	40.7	40.0
Distance between the tail of the projectile and the target surface (mm)	32.81	30.00	21.38	20.05	11.76	10.175	the tail of the projectile has entered the target	the tail of the projectile has entered the target
Error		8.56%		6.22%		13.5%		—

Table 6. Dimensions of the Penetration Hole of the Test Projectile

Projectile velocity (m/s)	917	940	1012
Entrance diameter of penetration hole (mm)	7.0	7.5	7.0
Exit diameter of penetration hole (mm)	7.0	7.7	8.0

Figure 3 shows the projectile and target configurations at t = 15, 20, 30, 40 μs after a steel target is hit by a steel projectile at 1000 m/s. During the penetration process, the steel projectile changes from a cylindrical shape to semi-spherical shape; the target plate deforms into an open cavity. The diameter of the cavity is 25 mm and is approximately equal to twice the projectile diameter; the diameter of the crushed projectile head is 21 mm, and the depth is 10 mm. The corresponding test data are presented in Table 7, and the shapes of the cavity and the crushed projectile are shown in the following photographs. It is interesting to note that the calculated results show a slight dent at the penetration tip of the projectile, which agrees with experimental observations.

Figure 3-1. Penetration Pattern for Fe → Fe 1000 m/s T = 15 μs, T = 20 μs

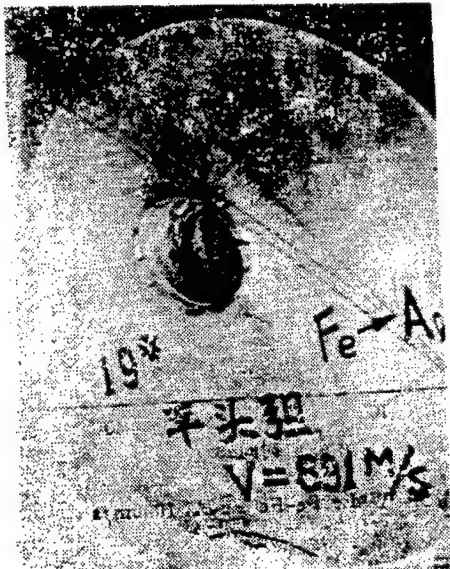Figure 3-2. Penetration Pattern for Fe Fe 1000 m/s T = 30 μs, T = 40 μs

Table 7

Projectile Velocity (m/s)	Diameter of the Crushed Projectile Head (mm)	Depth of the Crushed Projectile Head (mm)	Diameter of the cavity (mm)
890	19.2	10.5	20.2
approximately 900	19.1	10.7	20.4
920	19.3	10.8	21.1

Photograph 1

Photograph 2

Calculations for the Fe-Al case show that at t = 35 μs, the depth of penetration of the projectile is equal to the target thickness, whereas the depth of penetration for a steel target at the same instant is 14.8 mm. A test steel projectile traveling at 890 m/s can penetrate through a 20-mm-thick LY12 aluminum target, but it can only penetrate a depth of 14 mm into a steel target (see photographs below). Both calculations and test results show that the penetration resistance of a high-strength aluminum target is lower than that of a low-strength steel target.

Photograph 3. The Flat-Head Steel Projectile Used in the Test and the Residual Pellet After Penetration

Photograph 4. Projectile Penetrating Through the Target in the Fe-Al 891 m/s Case

2. Pressure Distribution Inside the Projectile and the Target During the Penetration Process

In the early stage of collision, shock waves are created in both the projectile and the target, but they disappear within 2-5 μs; therefore, their effect on penetration can be neglected. This result is consistent with that of Ref. [6]. The main effect of the shock waves is to create a fluid state and plastic fluid state in the material at the target surface and at the nose section of the projectile; this effect is reflected by the semi-spherical shape of the open cavity and the flipped lip in the target, and by the splattering of the material in the early stage of collision.

The penetration of the pellet creates a high-pressure region where the pressure p is much greater than the yield strength of the material Y_t. Therefore, in this region the material strength can be neglected, or the material can be considered to be in a general plastic fluid state. The calculated results for the three test cases are:

Photograph 5. Shape of the Penetration Cavity in the Fe-Fe 890 m/s Case

$W \rightarrow Fe$ at t = 2-30 σ, the high-pressure region is within a range approximately equal to twice the projectile radius in front of the projectile: $p = (10 \rightarrow 5) Y_t$

$Fe \rightarrow Fe$ at t = 5-20 μs, the high-pressure region is within a range approximately equal to twice the projectile radius in front of the projectile: $p = (6 \rightarrow 3) Y_t$

$Fe \rightarrow Al$ at t = 3-15 μs, the high-pressure region is within a range approximately equal to twice the projectile radius in front of the projectile: $p = (4 \rightarrow 1.5) Y_t$

3. Calculations of the Specific Internal Energies in Fe-Fe and Fe-Al Targets

(1) Within t = 1 μs, the maximum specific internal energy in the target I_{max} is located on the shock wave near the axis of symmetry. At t = 0.5 μs, the specific internal energy reaches its peak value: 3.01×10^5 J/kg for Fe-Fe and 3.02×10^5 J/kg for Fe-Al.

(2) When t = 1.5 μs, the maximum specific internal energy in the two-dimensional problem shifts from the target center to the right side of the projectile-target interface until the end of penetration.

(3) In the Fe-Fe case, from t = 5 to 30 μs, the average value of the maximum specific internal energy at the right side of the interface is

$$\bar{I}_{max} = 2.32 \times 10^5 J/kg, \quad \frac{\bar{I}_{max}}{I_m} = 17.9\%.$$

From the strength equation $Y = Y_0(1 - I/I_m)$, one can calculate that during the penetration process, the strength of the steel target decreases to $Y = 0.312 \times 10^9$ Pa.

(4) In the Fe-Al case, from $t = 3$ to 22.5 μs, ,

$$\bar{I}_{max} = 2.58 \times 10^5 J/kg, \quad \frac{\bar{I}_{max}}{I_m} = 36.8\%$$

and the strength of the aluminum target is estimated to be: $Y = 0.309 \times 10^9$ Pa.

4. Time Variation of the Penetration Velocity and the Depth of Penetration for the Three Test Cases

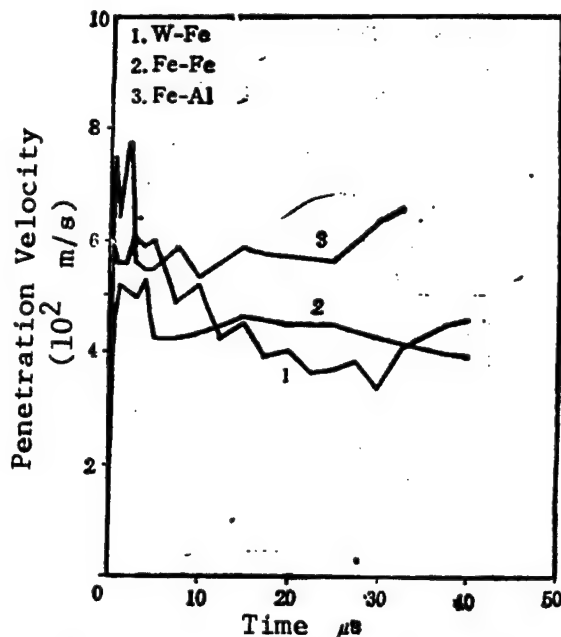The calculated results are shown in Figure 4 and Figure 5.

Figure 4. W-Fe, Fe-Fe, Fe-Al 1000 m/s

V. Analysis of Calculated Results

1. Analysis of the Penetration Capability of the Pellet

A comparison of the calculated W-Fe and Fe-Fe results shows that a tungsten projectile has greater penetration capability then a steel projectile (see the depth of penetration vs. time curve of Figure 5). This is consistent with the experimental results which show that a tungsten projectile traveling at 917 m/s penetrated a 20-mm-thick A3 steel plate, whereas a steel projectile traveling at 920 m/s did not.

The target plate parameters and projectile velocity used in the two calculations were identical, and the material strength of the projectile was similar; only the density
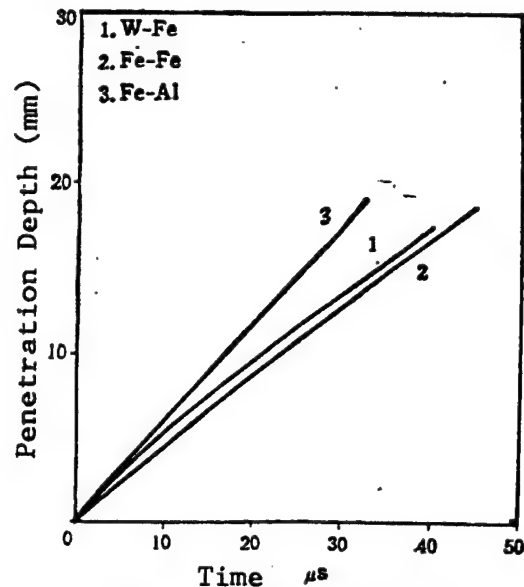

Figure 5. W-Fe, Fe-Fe, Fe-Al 1000 m/s

and the slender ratios of the projectiles were different. The ratio of kinetic energies of the two types of projectiles is:

$$\eta_1 = \frac{\frac{1}{2} m_W v_P^2}{\frac{1}{2} m_{Fe} v_P^2} = \frac{m_W}{m_{Fe}} = \frac{(0.4)^2 \cdot 4 \cdot 18}{(1.27)^2 \cdot 3 \cdot 7.85} = 0.303$$

Thus, the total kinetic energy of the tungsten projectile is only 30% of that of the steel projectile. It is known from Figure 4 and Figure 5 that the penetration velocities V_G obtained from the two calculations are approximately the same; hence the ratio of dynamic pressures exerted by the two projectiles on the target hole during the penetration process is:

$$\eta_2 = \frac{\frac{1}{2} \rho_W (v_P - v_G)^2}{\frac{1}{2} \rho_{Fe} (v_P - v_G)^2} \doteq \frac{\rho_W}{\rho_{Fe}} = \frac{18.0}{7.85} = 2.29$$

In other words, the dynamic pressure of the tungsten projectile is twice that of the steel projectile in penetrating the steel target. This analysis shows that the effectiveness of an armor-piercing projectile in penetrating a thick target is dependent on the pressure at the contact surface between the projectile and the target, not on the initial kinetic energy of the projectile. To achieve higher pressure at the contact surface and to enhance the effect of penetration, it is necessary to select an appropriate slender ratio and a relatively high projectile density to ensure that the projectile material has higher compressive strength and lower plasticity. When the
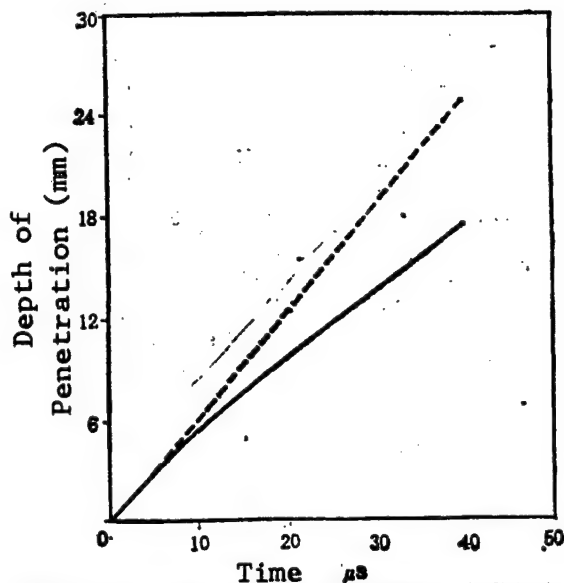
ADVANCED MATERIALS

Figure 6. Comparison of the W-Fe 1000 m/s Solution With the Ideal Fluid Solution—The dashed line denotes the ideal fluid solution

Figure 7. Comparison of the Fe-Fe 1000 m/s Solution With the Ideal Fluid Solution—The dashed line denotes the ideal fluid solution

target parameters and projectile material are fixed and only the projectile velocity v_p and slender ratio L_0/S_0 can be varied, then the penetration capability is determined by the initial specific kinetic energy of the projectile, i.e., the kinetic energy per unit area.

2. Analysis of the Penetration Resistance of the Target Plate

The calculated results of the Fe-Fe and Fe-Al cases show that under the action of an identical projectile, the penetration resistance of a high-strength aluminum target is lower than that of a low-strength steel target (see Figure 5). In an effort to analyze this phenomenon, a solution is obtained for each case by treating the projectile and target materials as an ideal incompressible fluid, as indicated by the dashed lines in Figure 6 - Figure 8. Comparison of this solution with the fluid elasto-plastic solution shows that for the Fe-Al case the two results are basically the same, whereas for the other two cases the results are different. This illustrates that during the penetration process an aluminum target is essentially in a fluid state.

It is known from the calculated results of specific internal energy that due to sensitivity to temperature, the strength of aluminum during the penetration process decreases to a level approaching that of steel. Therefore, the difference in penetration resistance between the two is primarily due to difference in density; the low-density aluminum target exhibits a fluid state, indicating that its penetration resistance depends primarily on the inertia of the material, and to a lesser degree on its strength. Only in the case of sufficiently high density the strength of the material begins to play an important role, as in the case of W-Fe, Fe-Fe. Therefore, the conventional approach of increasing the strength of an aluminum target to enhance its penetration
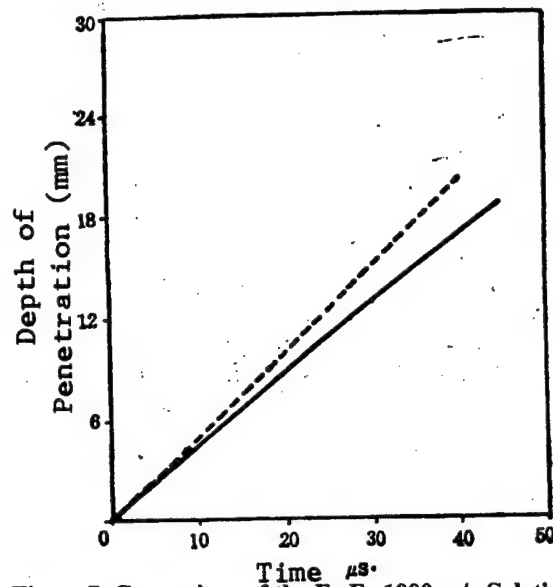
resistance is incorrect; an effective approach would be to change the thermal sensitivity of aluminum, and to develop a new light-weight material with high compressive strength, high temperature resistance and high malleability. (The residual pellet of the Fe-Al collision was coated with a layer of aluminum, indicating that the temperature at the projectile-target interface was higher than the melting point of aluminum.)
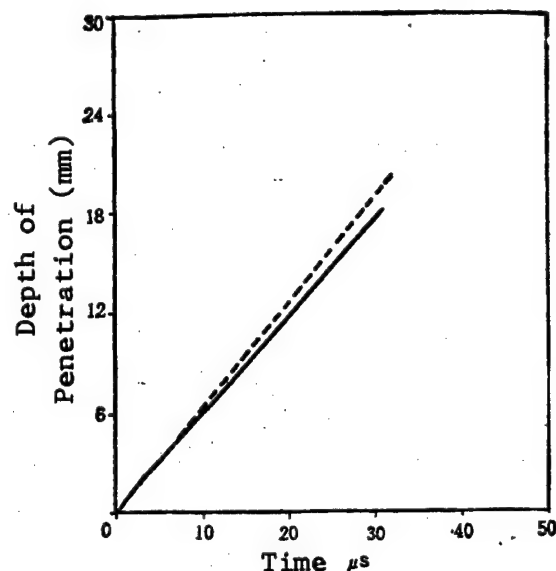

Figure 8. Comparison of the Fe-Al 1000 m/s Solution With the Ideal Fluid Solution—The dashed line denotes the ideal fluid solution

References

1. Zheng Zhemin, Duan Zhuping, et al., "Preliminary Analysis and Some Basic Information on Projectile Penetration Process," LIXUE QINGBAO [MECHANICS INFORMATION], 5, 6(1973).

2. Hageman, L. J., et al., "HELP Code Solution of Two Test Problems in Armor Penetration," AD. 725998 (1971).

3. Hageman, L. J. and Walsh, J. M., "HELP: A Multi-material Eulerian Program for Compressible Fluid and Elastic-Plastic Flow in Two Space Dimensions and Time," I, May (1977), AD. 726460, II, FORTAN listing of HELP.

4. Qin Mengzhao, Xie Chunsheng, et al., "Application Software for the Numerical Calculation of Two-Dimensional Non-Steady Fluid Elasto-Plastic Problems," SHUZHI JISUAN YU JISUANJI YINGYONG [JOURNAL ON NUMERICAL METHODS AND COMPUTER APPLICATIONS], 5, 3(1984) (Accepted by the U.S. Government as Technical Report AD-A159 392).

5. Xie Chunsheng, Qin Mengzhao, Liu Xiaoping, Lu Deye, "Improvement on HELP (CPG-LTDL) and Penetration Calculations," Xian Research Institute of Modern Chemistry, Internal Report.

6. Liu Xiaoping, Zhou Xiaohui, et al., "Numerical Simulation of Projectile Penetration at High Speed," Proceedings of the International Conference on High Dynamic Loads and Their Effects (1986).

Ion-Beam Mutation Produces High-Yield, Hardy Rice Varieties

*91P60028A Beijing RENMIN RIBAO in Chinese
24 Aug 90 p 3*

[Article by Miao Fanzu [5379 0416 0586]: "Ion-Beam Breeding Technique Jointly Developed by Two Research Institutes"]

[Summary] An ion-beam breeding technique has been developed by the Plasma Institute of the Chinese Academy of Sciences and the Paddy Rice Research Institute of Anhui Academy of Agricultural Sciences. Three varieties of short, high-yield and disease-resistant paddy rice were produced after 2 years of collaborative research. Among these three new varieties, Zhe-15 is the most valuable. The advantage of using an ion-beam as a light source is that ion beams can minimize seed damage and environmental pollution caused by other light sources and bring the mutation rate up from one-ten thousandth to 8 percent due to direct participation of carbon and nitrogen atoms from ion beams in DNA recombination and thus broaden seed mutation spectra through inducing mutations that cannot be achieved by isotop and laser irradiation. The ion-beam mutation project has been listed as a national key science and technology topic in order to further study the mechanism of mutation. The Ministry of Economy and Trade has invested 1.2 million U.S. dollars to construct an ion-beam breeding base.

Study on Pathogenicity and Toxicity of Salmonella typhimurium

*91P60028B Beijing ZHONGHUA
WEISHENGWUXUE HE MIANYIXUE ZAZHI
[CHINESE JOURNAL OF MICROBIOLOGY AND
IMMUNOLOGY] in Chinese Vol 10 No 4, Aug 90
p 255*

[Article by Wang Hongqi [3769 4767 2475], Wang Li [3769 7787], Zhang Weiguo [1728 4850 0948], and Wei Yanling [7614 3601 3781], People's Liberation Army 302 Hospital, Beijing]

[Summary] The adhesiveness, invasiveness, and the ability to produce cytotoxin and enterotoxin of 50 strains of Salmonella typhimurium have been studied. Forty-seven strains were found to be adhesive to HeLa cells, 41 of the 47 adhesive strains were found to invade the HeLa cells, and the invading bacteria were all found confined in the cytoplasm. The nonadhesive and low-adhesive strains (less than 10 percent of S.typhimurium-adhered HeLa cells found) were all tested to be noninvasive. Fifteen of the 50 strains produce cytotoxin that causes partial lysis and shrinkage of HeLa cells, four of the 50 strains studied were heat-stable enterotoxin (ST) positive, and three of the 50 strains were heat-labile enterotoxin (LT) positive. The ST or LT producers were found among the adhesive, nonadhesive, invasive and noninvasive strains; however, no one strain was detected that was able to produce both ST and LT at the same time. All 50 strains of S.typhimurium tested had a certain degree of adhesiveness, invasiveness, cytotoxin and enterotoxin-producing ability, but none was found to possess all these abilities in one cell.

Analysis of Oligonucleotides of Hainan Dengue Type II Virus

*91P60028C Beijing ZHONGHUA
WEIZHENGWUXUE HE MIANYIXUE ZAZHI
[CHINESE JOURNAL OF MICROBIOLOGY AND
IMMUNOLOGY] in Chinese Vol 10 No 4,
Aug 90 p 213*

[Article by Qin Ede [4440 6759 1795], Xu Pinfang [1776 0756 5364], Si Bingyin [0674 3521 6892], Huang Xiangrui [7806 4382 3843], Zhao Hong [6392 4767], Chen Wenzhou [7115 2429 3166], Yan Guozhen [7051 0948 3791]; Institute of Microbiology and Epidemiology, Chinese Academy of Military Medical Sciences: "Fingerprint Analysis of Oligonucleotides of Hainan Dengue Type II Virus; Project Supported by the National Natural Science Foundation of China"]

[Summary] The RNA fingerprint analysis method is used to determine the relationship between Chinese dengue type 2 (04 strain) virus from the Hainan epidemic area and the prototype (sub-B strain) virus from New Guinea. To date, three types (1, 2, and 4) of dengue virus have been identified by RNA fingerprint analysis; five topotypes of the type 2 strain were identified according to the degree of oligonucleotide homogeneity. To prepare the RNA gene group for analysis, the virus was first proliferated in single-layered mosquito cells (C6/36), concentrated with polyethylene glycol, purified by 5-25 percent sucrose or potassium tartrate-glycerol gradient centrifugation, lysed with protease K and then treated with phenol/chloroform/isopentanol. The two RNA gene groups obtained were then digested with ribonuclease T_1, labelled with ^{32}P and analyzed with polyacrylyl amide gel electrophoresis. The results showed that the fingerprint pictures of small oligonucleotides from the Hainan 04 strain and New Guinea sub-B strain resembled each other, and 31 of the 56 large oligonucleotides were shared by both strains. This indicates that the homogeneity of the large oligonucleotides from both strains was 55 percent and there is little genetic relationship between the Hainan 04 strain and the New Guinea prototype strain.

A Luminance Edge Detection Method Using Gradient of Gray Level for Synthetic Aperture Radar Imagery

[English abstract of article by Xu Wei and Chen Zongzhi of the Institute of Electronics, CAS, Beijing; MS received 17 Nov 89]

[Text] In multistage imaging processing for SAR digital imaging and the application of SAR imagery, it is often required to extract the luminance edge features of the SAR imagery. Already studied is extraction of the luminance edge features for the ordinary imagery produced by visible or infrared imaging system. The methods using gradient are effective for the extraction of the luminance edge features of ordinary imagery and are commonly used. Because the serious noise of coherent speckle exists in SAR imagery, some people believe that edge extraction using gradient for SAR imagery gives poor results. In this paper, a rather ideal method is derived for the extraction of luminance edge features for SAR imagery with the consideration of the characteristics of SAR imagery. This method uses the relative average gradient and combines detection with tracking.

References

1. Xu Wei, Chen Zongzhi, IEE Proceedings, Part F, 136 (1989), 1, 29-34.

2. W. K. Pratt, Digital Imaging Processing, John Wiley & Sons, USA, 1978.

3. S. C. Giess, Edge Detection in SAR Imagery Using Gradient Operators, RSRE Memo 3743, RSRE Malver, England, 1984.

Research on the Stabilities of Analog Electronic Neural Networks

[English abstract of article by Zeng Huanglin and Yu Juebang of the University of Electronic Science and Technology of China, Chengdu; MS received 18 Dec 89, revised 22 Mar 90]

[Text] A new method for analysing the stabilities of analog electronic neural networks is presented. The energy functions with clear and definite physical meaning are derived by introducing the static equivalent circuit models, which have expanded the Tellegen Theorem for application in circuit analysis. The method used to derive the energy functions of nets from first-order differential equations is valid for all first-order continuous autonomous systems. The stability analysis of cellular neural networks is made by the use of stationary cocontent theorem. Some results are instructive for the network circuit implementation.

References

1. J. J. Hopfield, Proc. Natl. Acad. Sci. USA, 79 (1982), 2554.

2. J. J. Hopfield, D. W. Tank, Science, 233 (1986), 625.

3. A. Desoer, S. Kuh, Basic Circuit Theory, McGraw-Hill, N.Y. (1969).

4. L. O. Chua, J. Frankin Inst., 296 (1973), 2, 9.

5. L. O. Chua, Lin Yang, IEEE, Trans. on CAS, CAS-35 (1988), 10, 1247.

6. K. Preston, Jr., M. J. B. Daff, Modern Cellular Automata: Theory and Application, New York Plenum (1984).

7. J. J. Hopfield, Proc. Natl. Acad. Sci. USA, 81 (1984), 3088.

Laser Separation of Uranium Isotopes

90FE0333C Beijing GUANGMING RIBAO in Chinese 10 Jul 90 p 1

[Article by Yang Jian [2799 0256]: "Important Progress in Laser Isotope Separation"]

[Text] Changchun, 9 July—Important progress has been made in laser isotope separation, "the technology of the next century."

Natural uranium is primarily uranium 238. The content of uranium 235, which is the nuclear fuel, is far below our requirement. Presently, uranium is primarily enriched by gaseous diffusion throughout the world. However, this requires large investment and consumes a great deal of power. Furthermore, it requires a large number of cascade separation devices. Laser separation, in one step, can concentrate uranium 235 to the level required for nuclear power-plant use. Moreover, it needs less capital, consumes less power and is safe and reliable. This is a high-tech effort with a very high degree of difficulty. So far, only a handful of countries have published some results.

After completing the fundamental experiment on "two-photon laser separation of uranium isotope" in 1985, the technical staff at the Institute of Applied Chemistry of the Chinese Academy of Sciences took over this national "Seventh 5-Year Plan" program. They explored the mechanism for a three-photon process in order to find a pattern for the separation process. In addition, various separation parameters were determined. For the first time, they conducted photo-ionization uranium laser separation experiments involving the resonance of three photons at three colors. The spectra obtained were at a world-class level in the 1980's.

On 9 July, this reporter saw the technical staff at the laser chemistry laboratory of Changchun Institute of Applied Chemistry conduct experiments to gather data for the final phase of the national "Seventh 5-Year Plan" program. Laboratory Directory Zhou Dafan [0719 1129 0416] said that they have obtained some energy level data that had never been reported before. A great deal of precious data on lifetimes of uranium atoms in excited states and on transition probabilities of uranium were also determined. In terms of experimental technique, they improved the technique for uranium evaporation. In the determination of pulse laser wavelength, they adopted a special spectroscopic technique. Spectral lines for laser-generated isotopes of uranium were selected experimentally.

Experts commented that this is another major breakthrough in laser isotope separation since the two-step laser ionization experiment. It has great significance to the development of the nuclear industry in China.

A GW Level High Power CO_2 Laser System

91FE0023A Shanghai ZHONGGUO JIGUANG [CHINESE JOURNAL OF LASERS] in Chinese Vol 17 No 6, Jun 90 pp 321-325 [MS received 12 Sep 88]

[Article by Zhuang Guoliang [8369 0948 5328], Yu Shusheng [0060 3412 3932], Niu Wanqing [3662 8001 7230], Du Longlong [2629 7893 7893], Li Mingfu [2621 2494 1381], and Jiang Hong [1203 5725] of Shanghai Institute of Optics and Fine Mechanics of the Chinese Academy of Sciences: "A GW Level High Power CO_2 Laser System"]

[Text] **Abstract**

This paper reports a newly developed GW level high power CO_2 laser system. A short laser pulse is cut out by a double Pockels cell electro-optical shutter from a hybrid CO_2 laser oscillator and amplified by a three-stage dual-path TEA CO_2 laser preamplifier, a two-stage TEA CO_2 laser preamplifier, a large aperture TEA CO_2 laser amplifier and an electron beam controlled terminal CO_2 laser amplifier. The output power is up to 3.2×10^9 W and the pulse width is 4 ns.

I. Introduction

Because of the obvious advantages of the CO_2 laser in terms of efficiency, reliability, reproducibility, manufacturing cost and operating expenses, countries with major economic strength have been developing high power CO_2[1,2] lasers, as well as high power neodymium glass lasers, for inertia confined fusion research. In order to study the interaction between 10.6 μm laser beam and matters and to conduct other related fundamental experiments, we developed a GW level high power CO_2 laser system. Experimentally, it was found to have a laser output power of up to 3.2×10^9 W and a pulse width of 4 ns.

II. System Structure and Principle

Figure 1 shows the high-power CO_2 laser system developed in this work. It uses a double Pockels cell electro-optical shutter to produce a short laser pulse (pulse width < 5 ns, adjustable) from a hybrid CO_2 laser oscillator. This laser pulse goes through a three-stage TEA CO_2 laser preamplifier, a two-stage TEA CO_2 laser preamplifier, a large aperture TEA CO_2 laser amplifier, and an electron beam controlled CO_2 laser terminal. Every part of the system is synchronously controlled by the control system.
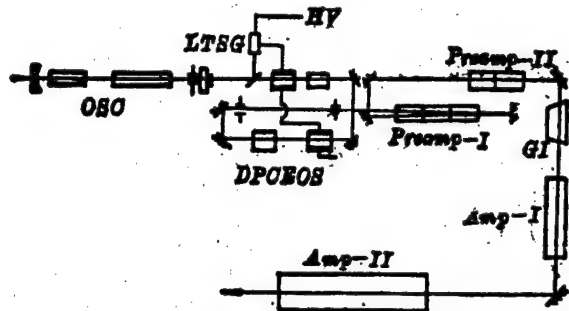
Figure 1. Sketch of the GW Level High Power CO_2 Laser System

OSC—hybrid CO_2 laser oscillator; DPCEOS—double Pockels cell electro-optical shutter; LTSG—laser triggered spark gap; Preamp-I—three-stage TEA CO_2 laser preamplifier; Preamp-II—two-stage TEA CO_2 laser preamplifier; GI—gas isolator; Amp-I—large aperture CO_2 laser amplifier; Amp-II—electron beam controlled CO_2 laser amplifier.

2.1 Oscillator

Operating in a single longitudinal mode, the output wave form of a TEA CO_2 laser pulse is smooth. It is suitable as an oscillator in a high power CO_2 laser system. In order to keep the laser operating in a single longitudinal mode, the low pressure gain portion in the cavity is increased. Furthermore, the following condition is met:

$$\Delta v_g \leq c/2L \qquad (1)$$

where Δv_g is the bandwidth of the gain of the laser medium, c is the speed of light and L is the length of the cavity. The operating pressure of the CW CO_2 laser tube was chosen to be 10 Torr and the gas ratio is $CO_2:N_2:He$ = 1:1:8. The expressions for collision broadening Δv_C, Doppler broadening Δv_D and FWHM (full width half maximum) of total broadening Δv_T are:[3]

$$\Delta v_0 = 5.76 \times 10^9 (\psi_{CO_2} + 0.73\psi_{N_2} + 0.6\psi_{He}) P_a (300/T)^{1/2};$$

$$\Delta v_D = 7.16 \times 10^{-7} v_0 (T/M)^{1/2};$$

$$\Delta v_T = (\Delta v_0^2 + \Delta v_D^2)^{1/2} \qquad (2)$$

where ψ_{CO_2}, ψ_{N_2}, ψ_{He}

are the ratios of CO_2, N_2 and He, respectively. P_a is the total pressure, T is temperature, and M is the molecular weight. Thus, Δv_C = 43 MHz, Δv_D = 61 MHz, and Δv_T = 75 MHz. If the length of the cavity is 2.7 m, then the spacing of longitudinal modes Δv = 56 MHz. When a CW CO_2 laser is

operating at a low gain, even there are two longitudinal modes between Δv_g, it still operates very stably in a single mode because of the large difference in gain.

The discharge volume of the TEA CO_2 laser in the hybrid CO_2 laser oscillator used[4] is 50 x 4.5 x 4.5 cm³. The gas composition ratio is $CO_2:N_2:He$ = 2:1:8. The discharge capacitance is 0.063 μf and the discharge voltage is 60 kV. The CW CO_2 laser has a triple tube structure. The inner diameter of the discharge tube is 20 mm and its length is 800 mm. The window is at Brewster's angle and is made of ZnSe. The resonance cavity is a stable cavity with a flat mirror and a concave mirror. The radius of curvature of the gold-plated concave mirror is 3.5 m. The output mirror is an uncoated germanium plate. A 7 mm diameter diaphragm for transverse mode selection is placed immediately next to the output mirror.

2.2 Double Pockels Cell Electro-Optical Shutter

In order to produce a short laser pulse, a double Pockels electro-optical shutter was developed[5] (see Figure 2). It consists of Pockels cells, a laser triggered shutter, polarizers, cables, a high voltage power supply, a beam splitter and reflection mirrors. GaAs crystal was used as the electro-optical shutter. It is 80 mm long and the half-wave voltage is 12.5 kV. Each polarizer is composed of four pieces of 80 mm diameter germanium plates. The angle of incidence is 76°. They are placed in a saw-tooth manner to prevent the beam from shifting from left to right. The laser triggered switch is of a standard 75 Ω impedance coaxial structure. A Ge lens with anti-reflective coating was used to focus the laser beam through a small hole on one electrode to the opposite electrode. The electrodes were 1 mm apart and the gap was filled with 14 atm of N_2. The pulse width was adjusted by adjusting the cable length in every section.
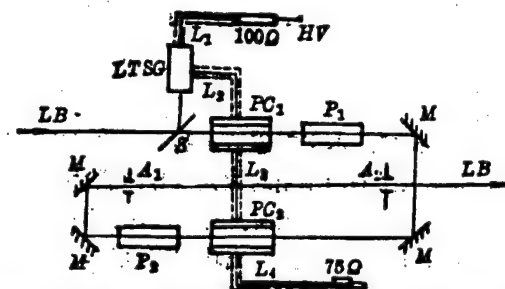
2.3 Preamplifiers

Figure 2. Structure of Double Pockels Cell Electro-Optical Shutter

LB—laser beam; LTSG—laser triggered spark gap; S—splitter; PC—GaAs Pockels cell; P—polarizer; L—cable; M—mirror.

The energy of the laser pulse from the double Pockels electro-optical shutter was amplified by going through preamplifiers. Each single stage of the preamplifier is identical in structure and size to the TEA CO_2 laser in the oscillator. In design, it was assumed that small signal

gain coefficient $g_o = 0.025/cm$, input laser intensity $I_{in} = 0.1$ mJ and output laser intensity $I_{out} = 1$ J. Then, from

$$\frac{I_{out}}{I_{in}} = e^{g_o L} \qquad (3)$$

the required gain length $L = 368$ cm. Since the gain length of the first stage TEA CO_2 laser is 50 cm, it requires eight stages. In reality, we first used a three-stage dual-path TEA CO_2 laser preamplifier and then followed by a two-stage TEA CO_2 laser preamplifier. In operation, the charging voltage and discharge capacitance are identical to those of the oscillator. However, the gas composition ratio is different. It is $CO_2 : N_2 : He = 3:2:8$ and the total pressure is 660 Torr. The window is made of NaCl 80 mm in diameter. It was placed at an angle of inclination of 8° to avoid parasitic oscillation due to end surface reflection.

2.4 Large Aperture TEA CO_2 Laser Amplifier

The laser pulse from the hybrid CO_2 laser oscillator went through the double Pockels electro-optical shutter and was then amplified by preamplifiers. The diameter of the beam gradually became larger in this process. Therefore, a relatively large aperture TEA CO_2 laser was chosen as a power amplifier in the middle stage.

The large aperture TEA CO_2 laser amplifier (see Figure 3) has a 280 mm diameter Plexiglass case. It is divided into two sections. Each section is 850 mm long. The cathode is made of hardened aluminum and the anode is a stainless steel net tightly fastened to the Plexiglass frame. An array of spark gaps, made of stainless steel plates, are used for pre-ionization. They are divided into five rows, 33 per row and 1 mm apart. Each row is 10 mm apart. There are five strips of copper foil opposite to these five rows of stainless steel plates. A 5 mm thick glass plate was used as insulation between the stainless steel plates and the copper foil. Each stainless steel plate and copper foil form a small capacitor. During instantaneous breakdown of these small capacitors, electrical sparks are generated on the glass surface to provide ultraviolet light for pre-ionization. This pre-ionization plate is approximately 25 mm away from the anode net. The surface of the aluminum cathode was sandblasted to prevent parasitic oscillation. NaCl windows are used on both sides of the device at a 5° angle with respect to the optical axis to avoid parasitic oscillation due to end surface reflection.

A three-stage Maxwell (?) generator was used for primary discharge. Its total capacitance is 0.047 µf. Preionization was done with a two-stage Maxwell generator. Its total capacitance is 0.07 µf. The primary discharge circuit and pre-ionization circuit are charged simultaneously in parallel to -30 to -35 kV. The delay time between primary discharge and pre-ionization could be adjusted to optimize the discharge. The working gas was $CO_2 : N_2 : He = 3:2:8$ and the total pressure was 560 Torr.

2.5 Electron Beam Controlled CO_2 Laser Amplifier

Whether an ultrashort high power laser pulse can be successfully obtained is determined by a suitable amplifier

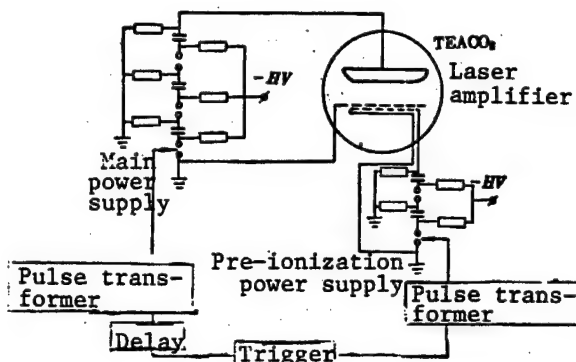Figure 3. Large Aperture TEA CO_2 Laser Amplifier

system. If ns range pulses are desired, the last amplifier must be designed to operate at atmospheric pressure or even higher pressure. Furthermore, the optical aperture must be large. To this end, a two-stage cold-cathode electron beam controlled CO_2 laser amplifier[6] with an effective discharge volume of 8 liters was developed as the last stage amplifier for this system (see Figure 4). The upper part of the figure is the cold cathode electron gun and the lower part is the laser gas discharge chamber. They are separated by a metal foil (0.02 mm titanium foil). The foil supported on an array of metal blades 14 mm apart and 10 mm in height to form an electron beam window. Its area is 860×80 mm^2. The cathode of the electron gun consists of six 750 mm long, 0.02 mm thick tantalum strips. The distance between the cathode and anode is adjustable and it is usually around 70 mm. Each stage of the electron gun has its own Maxwell (?) generator. They were triggered simultaneously by the spherical gap in the first stage. The output voltage is usually about 180 kV and the maximum energy storage capacity is 3.7 kJ.
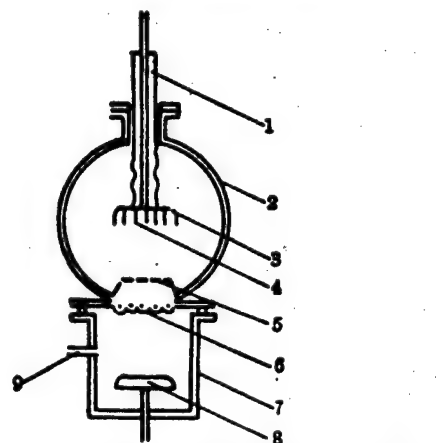

Figure 4. Cross-Section of Electron Beam Controlled CO_2 Laser Amplifier

1—Plexiglass lead wire jacket; 2—Stainless steel vacuum chamber case; 3—Electron gun cathode mask; 4—Electron gun cathode; 5—Electron gun anode; 6—Electron gun thin film window; 7—Laser box; 8—Main discharge anode; 9—Gas nozzle.

The outer case of the discharge chamber is made of Plexiglass. The inner surface was sandblasted to avoid oscillation. The anode is made of aluminum and its surface was sandblasted and its area is 920 x 120 mm^2 The cathode is an array of 2 mm diameter brass rods parallely spaced at 12 mm apart. Its area is 870 x 100 mm^2. It also serves as a protector for the electron beam window foil. The anode to cathode distance is adjustable (70-100 mm). Like the power source of the electron gun, the discharge chamber in each stage is connected to a set of capacitors. Both sets of capacitors are charged at the same time. Each set contains 15 0.45 μf, 50 kV capacitors.

2.6 Gas Insulator

In a high power CO_2 laser system, due to coupling between amplifiers, coupling between timing mechanism and amplifier, and internal reflection in amplifier, parasitic oscillation may occur. In order to overcome parasitic oscillation, a saturable gas optical insulator was developed. In order to prevent parasitic oscillation, the general rule is that the product of the gain g_o of each component to its gain length L should be less than a specific value.[7]

$$\Sigma g_o L < N \qquad (4)$$

The magnitude of N is determined by the operating parameters and the layout of the optical elements. From equation (4), if the small signal gain of each element can be effectively reduced, parasitic oscillation can be overcome. However, this will cause a decrease in the amount of energy accessible. An effective way is to add a saturable gas absorption chamber to the system to satisfy equation (4).

$$\Sigma g_o L - \Sigma \alpha p L' < N \qquad (5)$$

where α is the effective absorption coefficient (cm^{-1} Torr), p is the pressure of saturable gas (Torr) and L' is the length of the absorption chamber (cm).

The gas insulator developed in this work is a 60 mm diameter 150 mm long glass chamber with NaCl windows on both ends at Brewster's angle. Figure 5 shows the transmittance versus incident light intensity curve when filled with 2 Torr of SF_6. It shows that the absorption of the P(20) line at 10.6 μm by SF_6 is approaching saturation.

The small signal transmittance should be zero for an ideal saturable absorption chamber. For a large signal over a specific size, it is completely transmitted across. Thus, small amplitude parasitic oscillation can be suppressed and laser pulse output would not be lowered. In reality, it is not possible. Therefore, the location of the insulator becomes a very important issue. In our system, it was placed between the preamplifier and the large aperture amplifier to effectively suppress parasitic oscillation.
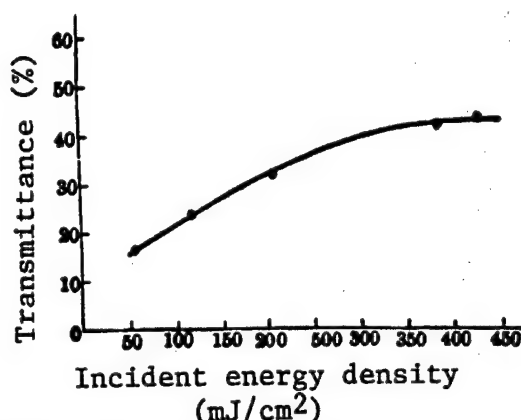

Figure 5. Saturation Characteristics of SF_6 (SF_6 pressure 2 Torr, absorption chamber length 15 cm)

III. Experimental Results

1. The energy of the output laser pulse from the hybrid TEA CO_2 laser oscillator was measured at 0.15-0.20 J with a carbon energy meter. The width of the output laser pulse from the oscillator was measured to be 400 ns with a photon drag detector and a SS-6200 oscilloscope.

2. A PT-1 laser energy meter was used to measure the energy of the laser pulse entering the first preamplifier after going through the double Pockels cell electro-optical shutter. It was found to be approximately 80 μJ. A 150 mm diameter carbon energy meter was used to measure the single pulse energy after the first two preamplifiers. It was found to be 0.5-0.8 J. The laser wave form is shown in Figure 6 [not reproduced]. After reshaping by the double Pockels cell electro-optical shutter, the laser pulse width is 4 ns.

3. The energy of the above laser pulse, after amplified by the large aperture TEA CO_2 laser amplifier, was measured to be 5-8 J.

4. Finally, after amplification by the electron beam controlled CO_2 laser amplifier, the energy of a single pulse was as high as 12.9 J and the laser power reached 3.2 x 10^9 W.

References

1. J. Jansen et al., Laser Focus, 16 (11), pp 76-84, 1980.

2. "IV Lekko Program," Annual Progress Report on Laser Fusion Program, September 1977-August 1978, Osaka University.

3. E. R. Pike, "High-Power Gas Laser," The Institute of Physics Bristal, London, 1975, 54: R. Loudon, "The Quantum Theory of Light," Clarendon Press, Oxford, 1978, 90.

4. Cai Yingshi et al., GUANGXUE XUEBAO [CHINESE JOURNAL OF OPTICS], 4 (2), 168, 1984.

5. Cai Yingshi et al., ZHONGGUO JIGUANG [CHINESE JOURNAL OF LASERS], 12 (8), 485 (2985.

6. Zhuang Dounan et al., ZHONGGUO JIGUANG [CHINESE JOURNAL OF LASERS], 7 (3), 33 (1980).

7. M. R. Green et al., J. Phys. D: Appl. Phys., 13, 1399-1404 (1980).

High-Power LF-11 Laser Passes Certification

90FE0333A Beijing GUANGMING RIBAO in Chinese 18 Aug 90 p 1

[Article by Yu Changan [0151 7022 1344], GUANGMING RIBAO reporter: "High-Power Laser Passes Certification"]

[Text] The LF-11, the highest power laser in China and the only one with frequency-doubling capability to perform practical experiments in physics, has been used in nearly 6000 experiments since 1985. It has produced a series of important results in cutting-edge high-tech areas such as inertial-confinement fusion (ICF) X-ray lasers and high-power laser atmosphere transmission. It passed certification by the Chinese Academy of Sciences and the Chinese Institute of Engineering Physics.

This 100,000 MW laser is an important piece of equipment in high-tech research in areas such as ICF and high-power laser technology. Based on the experimental data gathered over the past five years, its overall performance is fairly advanced. It is stable and reliable. The quality of its components is excellent and its high-efficiency frequency-doubling system is at a world-class level.

ICF is a cutting edge technical subject. In China, research on it began in the late 1970's. To obtain results in this subject not only has a great deal of significance to our defense but also has a tremendous impact on solving the energy problem for mankind. The materialization of goals in laboratory X-ray laser experiments would provide bright prospects, or even revolutionary changes, in areas such as biology, biomedical science, photolithography and ultra-high-resolution diagnostic techniques.
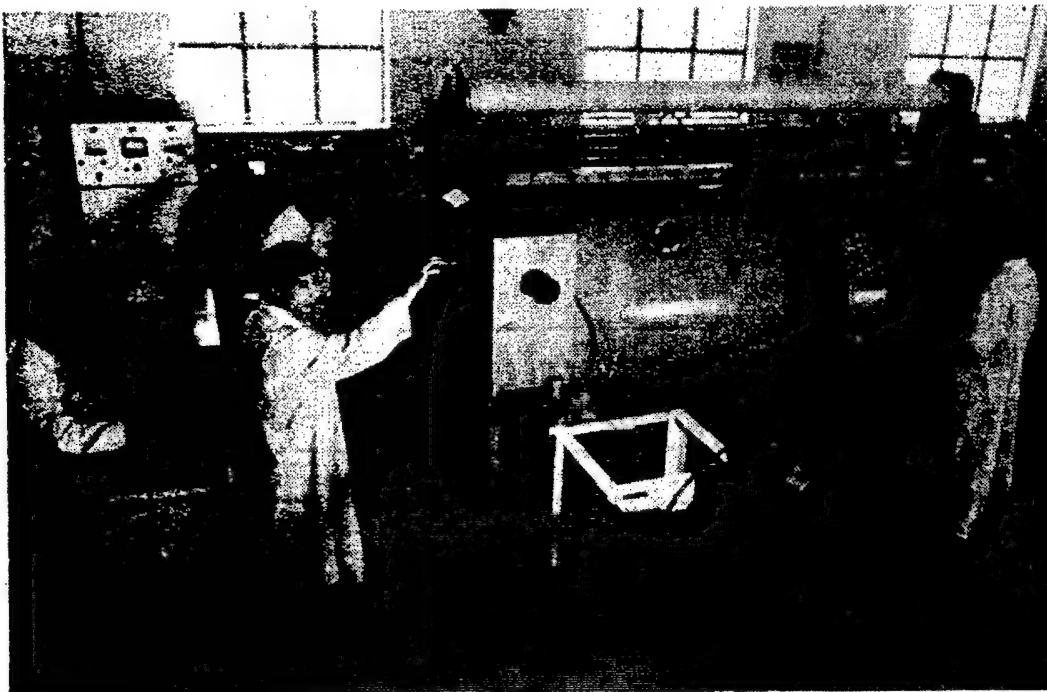
LF-11 was jointly developed by Shanghai Institute of Optics and Fine Mechanics and the Institute of Nuclear Physics and Chemistry of the Chinese Institute of Engineering Physics. It was totally designed, constructed, assembled, operated and upgraded by Chinese technical staff based on China's own industrial and technical strength.

Continuous CO_2 Laser R&D

90FE0333B Beijing RENMIN RIBAO [PEOPLE'S DAILY] (overseas edition) in Chinese 1 Aug 90 p 2

[Article (photograph taken) by Yu Chengqing [0151 3397 3237], reporter of the Xinhua News Agency]

[Text] The laser technology laboratory at Huazhong (Central China) University of Science & Technology has completed four key national projects in the past three years. The 10-kW-level continuous CO_2 laser they developed received the technical recognition award for the "Seventh 5-Year Plan." Experts believed that "It signifies our entrance to the world-class level in high-power laser research." The photo shows researchers operating the 10-kW continuous CO_2 laser.

LASERS, SENSORS, OPTICS

Compression Experiment of Neon-Filled Microballoons Irradiated by Two 1.06-μm Laser Beams

[Article by He Shaotang [0149 4801 1016], Yang Xiangdong [2799 0686 2639], Ding Yaonan [0002 5069 0589], and Cheng Jinxiu [2052 6855 4423] of the Southwest Institute of Nuclear Physics and Chemistry, Chengdu, and Zhang Tanxin [1728 6009 9515] of Beijing Institute of Applied Physics and Computational Mathematics: "Compression Experiments of Neon-Filled Glass Microballoons Irradiated by Two 1.06-μm Laser Beams"]

[Text] Abstract

Ne-filled microballoons were used for implosion compression experiments on the Shenguang ["Magic Light"] laser (10^{12} W). Results show that symmetric implosion compression was achieved by heating the target with the laser. The electron density inside the core reached 10^{23} cm^{-3} and the mean implosion velocity was 3.3×10^7 cm/s.

PACC: 0630E; 5270; 3270; 5200.

I. Introduction

In ICF (inertial confinement fusion) experiments, one of the most important tasks is to study compression in targets. This involves the use of several laser beams (at least two) to directly heat up a spherical target containing fusion fuel. The fuel is heated and compressed to trigger the fusion reaction. By diagnosing various phenomena, one can study the physics associated with this implosion compression. Because this study can provide a large amount of physical data, including electron temperature in the plasma, electron density, neutron production, symmetry and homogeneity of compression and fluid dynamic properties of compression, this experiment can help us understand the physics associated with ICF in more detail. This will allow us to continuously improve and create the conditions to make a controllable fusion reactor a reality in the near future.

Since the mid-1970s, many foreign laboratories have conducted a large number of studies on implosion compression. We performed a compression experiment using fusion targets on the Shenguang laser (10^{12} W). Symmetric implosion compression was achieved. The internal electron density was 10^{23} cm^{-3} and the mean implosion velocity was 3.3×10^7 cm/s.

II. Experimental Conditions and Diagnostic Method

The experiment was carried out at the Shenguang laser facility. It is a dual-beam high-power pulsed neodymium-glass laser (1.06 μm). In the experiment, two laser beams, one from the south and another from north, were used. The synchronization error of the two pulses is less than 10 ps. The energy of each beam is 15 - 100 J. The energy difference between the two beams varies from 1 to 28 percent compared to their mean energy. The laser pulse is approximately 100 ps wide and the signal-to-noise ratio is 10_4 - 10^7. A f/1.7 lens was used for focusing and the focal spot diameter on the target was approximately 120 μm.

The glass microballoon used in the experiment has a diameter of 80 - 106 μm. The wall thickness is 0.7 μm. The eccentricity of the microballoon is 6.7 - 10 percent. It was filled with Ne gas at a pressure of approximately $6.08 \times 10_5$ Pa.

Experimentally, an X-ray pinhole camera was used to diagnose the symmetry and volumetric compression ratio of the compression. The diameter of the pinhole is 16 μm. It was made of 10-μm-thick Ta foil. X-ray images were recorded on Tianjin II X-ray film. An Al-plated (360 nm thick) plastic film (2 μm thick) is used as a light-shielding layer. Two pinhole cameras were used in the experiment. Both were mounted perpendicular to the axis of the laser. One had a 1.7-cm object distance and 20-cm image distance and the other had a 0.8-cm object distance and 7.6-cm image distance.

An X-ray streak camera was used to measure the dynamic characteristics of implosion compression. The time resolution of the streak camera is 15 ps and the energy-response region is 1 - 10 keV. A 20-μm-diameter pinhole was placed in front of the streak camera. The pinhole is 3.5 cm from the target and 46.5 cm from the slit of the camera. Since the slit has a finite width, the image resolution is 41 ps in time and 20 μm in space. The most difficult part of the experiment was to adjust the position of the pinhole because the slit, pinhole and target had to be on the same straight line. The streak camera was placed at a 90° angle with respect to the laser beam. A laser theodolite was used for alignment.

Two crystal spectrometers were used to measure the X-ray spectra of the plasma. One of them was installed at a 60° angle with respect to the laser beam using a RAP (2d=2.612 nm) flat crystal, covering a range from 0.49-1.2 nm, to measure the emission spectra of the glass (Si and Na). The other was placed at 85° with respect to the laser beam using a KAP (2d=2.6632 nm) flat crystal, covering a range from 0.75-1.3 nm, to primarily measure the emission spectra of the Ne plasma. The crystal is 48 mm long, 10.5 mm wide and 1.5 mm thick. Crystal diffracted X-rays were recorded on Kodak AA-5 film. Two layers of 400-nm-thick Al coating were used in front of the film to block off visible light. The structure of the crystal spectrometer is shown in Figure 1.
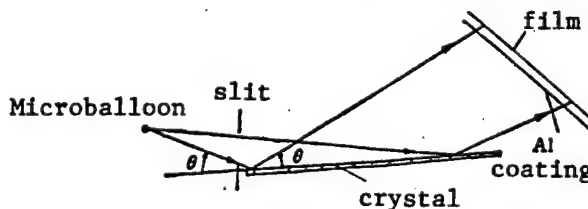

Figure 1. Schematic Diagram of Crystal Spectrometer

X-ray diffraction on the crystal obeys Bragg's law:

$$k\lambda = 2d \sin \theta \quad (1)$$

where λ is the wavelength, k is the order of diffraction, 2d is the lattice constant, and θ is the angle between the X-ray and the crystal plane which is the diffraction angle.

By analyzing the X-ray spectra, it is possible to obtain the electron temperature and post-compression electron density in the plasma.

III. Experimental Results

1. Compression Symmetry

The density distribution of the extent of exposure on the film from the pinhole camera can illustrate the symmetry of compression. Figure 2 shows the density distribution with target 2118. From this figure, it is essentially symmetric.
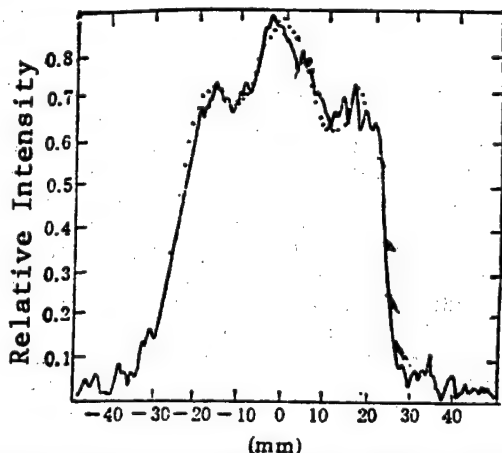

Figure 2. Density Distribution and Simulation of Pinhole Camera Picture of Target 2118. Abscissa is magnified 50 times.—— experimental, ... simulation.

2. Volumetric Compression Ratio

The ratio of initial Ne volume to compressed volume is defined as the volumetric compression ratio. It is denoted as σ:

$$\sigma = V_0/V \quad (2)$$

where V_0 is the initial volume which is obtained by measuring the diameter and wall thickness of the microballoon. V is the compressed volume, and is determined by the FWHM [full width at half maximum] of the center peak of the density track distribution.

There are three peaks in the density track curve. It is believed that the two peaks on either side are caused by the X-rays from the glass shell and the middle peak is due to X-rays from the compressed Ne plasma. It was experimentally confirmed that the tighter it was compressed, the more serious the overlap of the peaks became. The profile of the center peak was found by a multi-peak deconvolution method to obtain its FWHM value. The values of three

Gaussian distribution functions were superpositioned in this analysis. For target 2118, the density distribution is

$$f(x) = 0.64\exp\{-[(x + 18)^2/2 \cdot 6.5^2]\}$$
$$+ 0.84\exp[-x^2/2 \cdot 7.9^2]$$
$$+ 0.67\exp[-(x - 19)^2/2 \cdot 6.3^2].$$

Therefore, the FWHM of the center peak is 18.56 mm. Because of a 50-fold magnification of the densitometer, the actual FWHM is 0.371 mm.

The diameter of the pinhole is 16 μm. To some extent, it stretches the image. Based on Figure 3, the amount of stretch is $L = \varphi a + b$ over a = 0.16 mm. The magnification factor of the pinhole camera is 9.5. After taking these two factors into account, the diameter of the center peak, i.e., the diameter of the compressed Ne microballoon, is 21.36 μm.

$$\sigma = \left(\frac{87.6}{21.36}\right)^3 = 68.4$$

Hence, the volumetric compression ratio is .

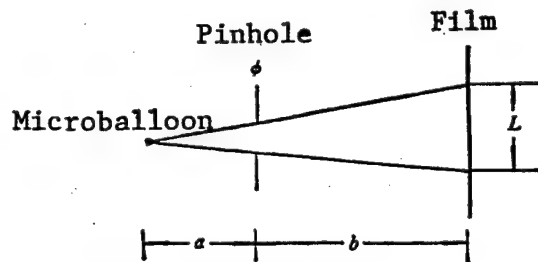**Figure 3. Image Stretching by Pinhole**

3. Determination of Electron Temperature

The ratio R_3 of H-like to He-like Ne intensity is used to determine electron temperature T_e.

$$R_3 = I(1s - 3p)/I(1s^2 - 1s^23p) =$$
$$\frac{A^H_{1-3}(h\nu) \cdot N^H_{3p}}{A^{He}_{1-3}(h\nu) \cdot N^{He}_{3p}}, \quad (3)$$

where I is spectral line intensity, A is Einstein's constant, N is the density of ions in the upper energy level involved in the transition, H and He represent H-like and He-like, respectively; and hν is the X-ray emission.

The system is considered to be in near thermal equilibrium. Then, equation (3) can be transformed into the following by using the Boltzmann distribution and Saha's equation:

$$R_3 \approx 3(N_i^{+10}/N_i^{+9})\exp(-0.029/T_e), \quad (4)$$

where T_e is expressed in keV, and $N^{+10}{}_1/N^{+9}{}_1$ is the H-like to He-like Ne ion density ratio which can be calculated using the corona model. We did not perform the calculation. Instead, we directly used the curve calculated by Yaakobi[1] (see Figure 4) to determine electron temperature T_e. Figure 5 is the spectrum of target 2118 obtained with the crystal spectrometer. From Figure 5, we get $I(1s-3p)/I(1s^2-1s3p) = 4.17$. From Figure 4, the electron temperature $T_e = 375$ eV.
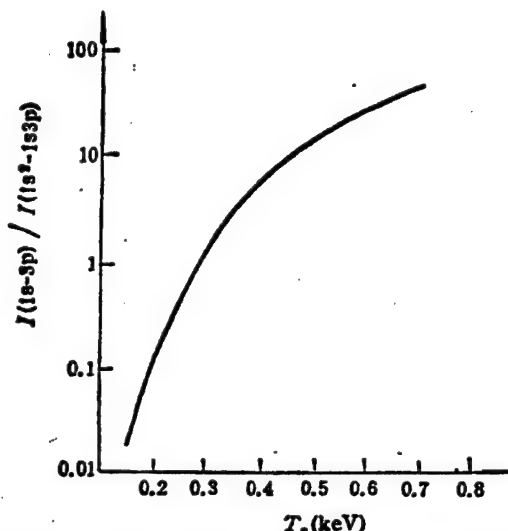

Figure 4. Line Intensity vs. Electron Temperature
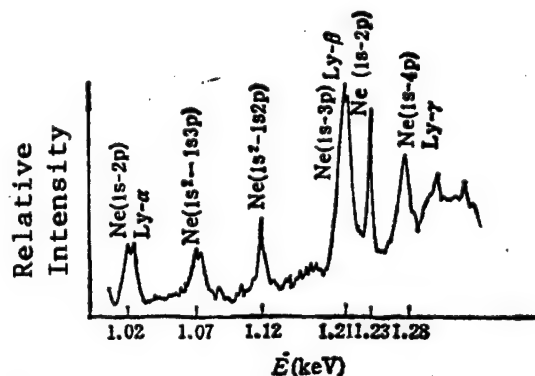

Figure 5. X-ray Spectrum of Ne-Filled Microballoon 2118

4. Determination of Electron Density

The broadening of the spectral line is used to determine electron density. From Figure 5, the Lyman lines of Ne (Ly-α(1s-2p), Ly-β(1s-3p), Ly-γ(1s-4p)) are much broader than Na lines. This is due to Stark broadening and Doppler broadening of the dense plasma. In laser compression studies, it is common in other countries to determine the electron density after compression based on theoretical modeling of the profile of spectral lines.[1-5] In China, Hou Qing [0186 8641] and Li Jiaming [2621
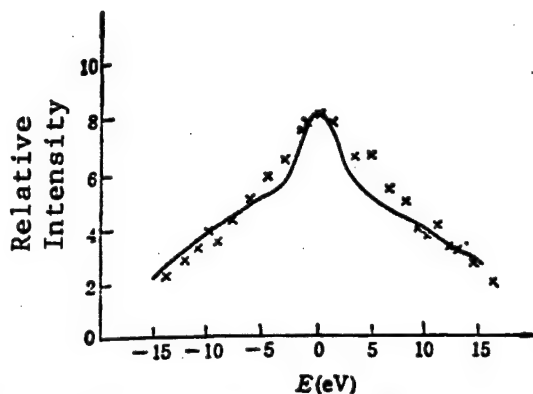

Figure 6. Theoretical (solid curve) and Experimental (x) of Ly-γ (9.7 Angstroms), $T_e = 400$ eV, Ne $= 10^{23}$ cm^{-3}

1367 2494] have done some theoretical work in this area.[6] After obtaining our experimental data, we also conducted some numerical simulation. We adopted the concept introduced in reference [5]. At a given electron temperature and electron density, the Stark equations for the first four H-like Lyman lines, i.e., Ly-α, Ly-β, Ly-γ, and Ly-δ, were given. In addition, the Doppler effect of these ions was also taken into consideration in order to derive plasma-emission spectral line equations. In this numerical simulation, the microscopic electric field distribution function was calculated based on the method reported in reference [4]. The Stark broadening equation was obtained based on electron collision and linear Stark effect of quasi ion state. Figures 6 and 7 show the numerical results of Ly-γ and Ly-β lines. From these results, it was determined that electron density Ne $= 10^{23}$ cm^{-3}. Assuming that on average, 8.5 electrons are stripped from every atom after Ne is heated, the pressure inside the microballoon is 6.08×10^5 Pa, and the compression ratio is 72.7.
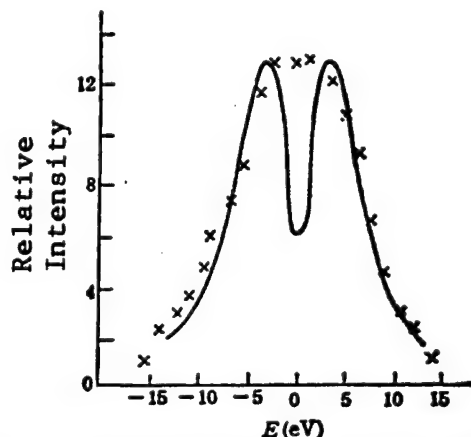

Figure 7. Theoretical (solid curve) and Experimental (x) of Ly-β (10.239 Angstroms), $T_e = 400$ eV, Ne $= 10^{23}$ cm^{-3}

From Figure 5 we can see Ly-α has a double peak. This effect cannot be explained by our computation because of self-absorption of the plasma. This phenomenon is

called self-reversal. In order to conduct numerical computation of self-reversal, self-absorption of the high-density plasma must also be taken into account.

5. Determination of Implosion Velocity

From the pictures taken by the pinhole streak camera, the implosion time is 150 ps and the mean implosion velocity is 3.3×10^7 cm s^{-1}.

IV. Conclusions

Compression experiments on Ne-filled microballoons were successfully performed on the Shenguang laser. Good results were obtained. Table 1 shows the data for three targets; this data helped us gain a deeper understanding of implosion dynamics.

Table 1. Results of Three Targets

Target Number	Diameter μm	Ne pressure (Pa)	Laser Energy on Target Surface South/North (J)	Laser Pulse Width (ps)	Volumetric Compression Ratio σ	Electron Temperature Te (eV)	Mean Implosion Velocity (cm x s^{-1})	Core Electron Density (cm^{-3})
2118	89	6.08×10^5	32.0/30.7	approximately 100	68.4	375	3.3×10^7	1×10^{23}
2220	89	6.08×10^5	41.9/47.9	99	50.1	425		0.8×10^{23}
2425	101	6.08×10^5	47.7/51.1	94	57.3	380	3×10^7	0.9×10^{23}

References

1. B. Yaakobi, et al., PHYS. REV., A19(1979), 1247.

2. H. R. Griem, et al., PHYS. REV., A19(1979), 2421.

3. J. D. Kilkenny, et al., PHYS. REV., A22(1980), 2746.

4. R. J. Tighe and C. F. Hooper, Jr., PHYS. REV., A15(1977), 1773.

5. B. Held, et al., PHYS. REV., A29(1984), 896.

6. Hou Qing and li Jiaming, WULI XUEBAO [ACTA PHYSICA SINICA], 37(1988), 1972.

A Non-Linear Neural Network Suitable for Optical Implementation and Its Monte Carlo Algorithm

[Article by Huang Wuqun [7806 0063 5028], Gao Chengqun [7559 2052 5028], Chen Tianlun [7115 1131 0243], and Hu Beilai [5170 0554 0171] of the Department of Physics, Nankai University and Zhang Yanxin [1728 1693 3512] of the Institute of Modern Optics of Nankai University: "A Non-Linear Neural Network Suitable for Optical Implementation and Its Monte Carlo Algorithm"]

[Text] **Abstract**

The storage capacity α_c and addressability of a non-linear neural network suitable for optical implementation is studied by computer simulation in this paper. A Monte Carlo algorithm has been proposed to improve its synaptic interconnection matrix. Numerical analysis showed that the modified neural model has significantly improved storage capacity and addressability.

Key words: Non-linear neural network, storage capacity, addressability, Monte Carlo algorithm.

I. Introduction

In the area of model recognition, the present computer cannot meet our needs. It is far behind human intelligence. For example, a computer cannot compete with a 3-year-old child in recognizing a jumping fish. Therefore, to develop a neural network computer to simulate the human brain has been a long-sought-after goal for many years.

Since Hopfield[1] introduced his neural network model in 1982, many modifications have been made. In addition, several other neural network models have been proposed.[2] The common features of all the neutral network models is the synaptic interconnection between neurons and the iterative succession of the network. The collective function of a large number of neural networks thus produced may have some functions of the human brain, such as distributive storage, association and memory, and tolerance to errors in the event some neural networks malfunction or make mistakes. For

instance, in Hopfield's model the interconnection weight or synaptic interconnection matrix element between the ith and jth neuron is

$$T(i, j) = \begin{cases} \sum_{\mu=1}^{M} \xi_i^\mu \cdot \xi_j^\mu, & i \neq j \\ 0 & i = j \end{cases} \qquad (1)$$

where ξ^μ_i is the state of the ith neuron in the μth storage mode, which is +1 (stimulated) or -1 (suppressed). M is the number of storage modes and n is the total number of neurons. From (1) we know that T(i,j) covers the range [-M, +M].

Let us consider this neural network as a kinetic system with N spins. After giving an arbitrary initial state, the system evolves according to the following kinetic pattern:[3]

$$S_i(t+1) = \text{Sgn}\left[\sum_{j=1}^{N} T(i, j) \cdot S_j(t)\right], \quad 1 < i, \ M < N \qquad (2)$$

where $S_j(t)$ is the state of the jth neuron after t times of interations. Sgn is a sign function, i.e.:

$$\text{Sgn}(x) = \begin{cases} 1, & x > 0 \\ 0, & x = 0 \\ -1, & x < 0 \end{cases}$$

When M << N, the system converges to a storage mode which is closest to the initial state.

The special features of using optical technology in a neural network model include high data capacity, fast computation speed and freedom from wiring problems. However, it has its shortcomings as well. For example, the dynamic range of the optical recording medium is small, the numerical accuracy is comparatively poorer, and it is difficult to express the sign of a number and to set up the input and output interfaces. As an example, Psultis[4] used an optical matrix multiplication technique to achieve an optical neural network. The numerical values of the interconnection matrix elements are expressed by the transmittance of an optical plate. When M is large, the dynamic range of the optical plate cannot meet the need for (2M+1) shades of gray.

Van Hemman[5] proposed and studied a non-linear neural network model. Its synaptic interconnection matrix is

$$J(i,j) = \varphi[T(i,j)] \qquad (3)$$

where T(i,j) is an element of the interconnection matrix in the Hopfield model or a linear neutral network. $\varphi(x)$ is an arbitrary non-linear function of x.

As a special case of a non-linear neural network, when

$$J(i, j) = \begin{cases} \text{Sgn}\left(\sum_{\mu=1}^{M} \xi_i^\mu \cdot \xi_j^\mu\right), & i \neq j \\ 0, & i = j \end{cases} \qquad (4)$$

the value of the interconnection matrix J(i,j) is limited to +/- 1 or 0. Furthermore, it is independent of the number of storage mode M in the network. The interconnection matrix can easily be materialized by an optical plate. In addition, the matrix element J(i,j) is either +1 or -1 which reduces the iteration process to simple logic operations. This is also a desirable factor for computer processing. Therefore, it is a non-linear neural network suitable for optical implementation.

Van Hemman[5] solved the fixed point equation of a non-linear neural network and studied the stability of the solution from a theoretical standpoint. This work uses computer simulation to study the storage capacity and addressability of a non-linear neural network that is suitable for optical implementation. Moreover, a Monte Carlo learning algorithm is presented to optimize the interconnection matrix. Computer simulation showed that both storage capacity and addressability of the network have been significantly increased after the interconnection matrix is modified by the learning process.

II. Computer Simulation and Results

Computer simulation of this non-linear neural network model suitable for optical implementation was performed on an M-340 computer. The results obtained are as follows:

1. Storage Capacity α_c

In order to explain what storage capacity α_c is, let us define the degree of overlap between two states S and S' of the neural network q(S,S'),[3] which reflects the similarity between these two modes:

$$q(S, S') = \frac{1}{N} \sum_{i=1}^{N} S_i \cdot S_i' \qquad (5)$$

For M random storage modes ξ^μ, μ = 1, 2, ..., M, any element of the interconnection matrix of the neural network J(i,j) can be calculated based on (4). A random mode is that its first ξ^μ has an equal probability of being +1 or -1. By substituting T(i,j) in equation (2) with J(i,j), the iteration equation of the non-linear network is obtained. We can choose any storage mode ξ^μ as the initial mode. Once it is stabilized after state iteration, it is possible to calculate the overlap q between the stable mode and ξ^μ. For different M, 1,000 sets of different

random storage modes are chosen. The average overlap $<q>$ of all possible storage modes as the initial mode can be then determined. Figure 1 shows the average overlap versus parameter $\alpha = (M/N)$ curve when $N = 100$. It is apparent that when the total number of neurons are fixed, $<q>$ decreases with increasing M. The value of α at $<q> = 0.99$, denoted as α_0, is defined as the storage capacity of the neural network. It represents the amount of information that the neural network is capable of recognizing correctly in its initial input mode. Within the accuracy of addressable reappearance, the maximum number of storable modes is $M = \alpha_c N$.
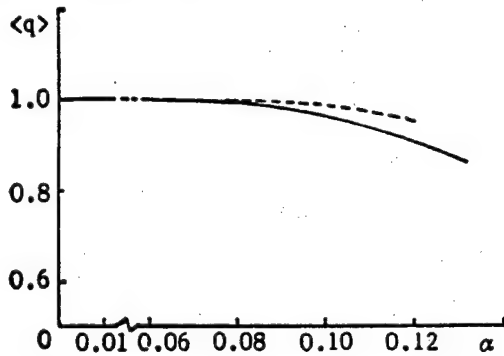

Figure 1. The dependence of average overlap $<q>$ on α, solid: before learning; dashes: after learning.

Figure 1 shows that $\alpha_c = 0.08$ for the non-linear neural network not modified by the Monte Carlo learning algorithm (solid curve). It is less than the 0.138 storage capacity obtained by Amit[6] using the Hopfield model.

In order to determine the relation between α_c and the number of neurons, the values of α_c corresponding to N = 25, 50, 100, 200, 400 and 800 were obtained by simulation in this work. Within this range, α_c showed no dependence upon N.

2. α_c vs. P_n Curve and Addressability

In order to evaluate the addressability of a non-linear neural network suitable for optical implementation under noise, we replaced N' components in each storage mode with equal number of random numbers +/- 1 and used it as the initial mode with a specific noise ratio of $P_n = (N'/N)$. Based on the simulation technique described earlier, $<q>$ was determined at different α. Figure 2 shows the α_c vs. P_n curve.

Obviously, the system can always correctly recognize ($<q> \geq 0.99$) the initial mode to the left of the curve. To the right of the curve, however, it cannot recognize it perfectly ($<q> < 0.99$). From Figure 2 we can see that this non-linear neural network model suitable for optical implementation is relatively resistant to noise.

III. Monte Carlo Algorithm

As Amit and Gutfreund[6] pointed out, the storage capacity in the Hopfield model is limited by the overlap
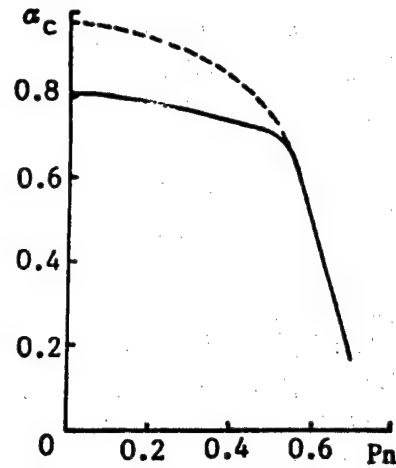

Figure 2. Influence of input noise P_n onto α_c, solid: before learning; dashes: after learning.

between storage modes. This also limits the storage capacity of a non-linear neural network suitable for optical implementation.

In 1988, Gardner and Derrida[7] conducted an analytical study on the synaptic interconnection matrix $J(i,j) = +/- 1$. Their method treated each synaptic interconnection matrix element $J(i,j)$ as a spin. The synaptic interconnection matrix corresponds to a spin state unordered set: $J(i,j)$ and the distribution function of the system is

$$Z(\beta) = \langle \exp[-\beta \cdot P_{wi}(\{J(i, j)\})]\rangle, \qquad (6)$$

where $< >$ is an average over all the states in the spin system, $\beta = (1/T)$, and T is the temperature of the spin system. P_{wi}(unordered set: $J(i,j)$) is a quantity proportional to the probability that the ith neuron state is erroneous and will be simply expressed as P_{wi} later.

$$P_{wi} = \sum_{\mu=1}^{M}\left[1 - \Theta\left(\xi_i^{\mu}\sum_{j\neq i}^{N}J(i, j)\xi_j^{\mu} - K\right)\right], \qquad (7)$$

where $\Theta(x)$ is defined as:

$$\Theta(x) = \begin{cases} 1, & x>0 \\ 0, & x<0 \end{cases} \qquad (8)$$

As far as storage mode ξ^{μ} is concerned, the local field acting on the ith neuron h^{μ}_i is (for convenience it is off by a constant factor N):

$$h_i^{\mu} = \sum_{j\neq i}^{N}J(i, j)\xi_j^{\mu}, \qquad (9)$$

Equation (7) indicates that the state of the ith neuron in ξ^{μ} would not make any mistakes only when $\xi^{\mu}_i h^{\mu}_i > K$. K is proportional to the threshold of the neuron.

Gardner, like Derrida, employed the replica method to analyze the solution of the spin state corresponding to

minimum <P> and its stability. The conclusion was that unordered set: $J^*(i,j)$ corresponding to minimum $<P_{wi}>$ must be solved numerically and is not stable.

In this work, Monte Carlo algorithm is widely used in statistical mechanics and lattice theory[9] in the spin system unordered set: $J(i,j)$ whose distribution function is equation (6) in order to obtain the spin state unordered set: $J^*(i,j)$ which has the smallest P_{wi}. It is used to build a synaptic interconnection matrix for a modified neural network which is suitable for optical implementation. This method to obtain J is called the Monte Carlo learning algorithm.

The Monte Carlo learning algorithm is as follows. The interconnection matrix $J(i,j)$ from equation (4) is used as the initial spin state unordered set: $J(i,j)$. Choose K = 0, 1N (N = 100). Use equation (7) as the Hamiltonian of the spin system and perform Monte Carlo simulation for T = 0 to find the unordered set: $J^*(i,j)$ corresponding to P equal to zero.

Using $J^*(i,j)$ to replace $J(i,j)$ as the interconnection matrix of the neutral network, the following improvements take place.

1. Improved Storage Capacity

After replacing J with J^*, computer simulation showed that the modified model does have a higher storage capacity α^*_c. The magnitude is dependent upon the storage mode and the number of neurons. Generally, when N < 100, the smaller N is the more significant the increase is. α^*_c is approximately 1.2-2.5 times of α_c. The dotted line in Figure 1 shows the average of 1,000 storage modes when N = 100 and $\alpha^*_c \approx 0.10$.

2. Improved Addressability

The addressability of the modified model in the presence of random noise was calculated to obtain the α^*_c vs. P_n curve which is shown as the dotted line in Figure 2. It clearly shows that the addressability of the model has been enhanced significantly after learning when α is large.

IV. Conclusions

The interconnection matrix element of the non-linear neural network studied in this work, $J(i,j) = +/- 1$, is independent of the number of storage modes. This is not only suitable for implementation with optics but also with microelectronics. Because its iteration process only requires logic operations, the speed of computation can be drastically increased.

Numerical analysis shows that the storage capacity of this model is slightly lower than that of the Hopfield model. Nevertheless, its noise resistant addressability is higher than that of the Hopfield model. Because it is easier to implement a large neuron number N with optical technology, the fact that α is small is not a serious problem in practice. As for the negative value in the interconnection matrix, it can be avoided by introducing

$J'(i,j) = J(i,j) + 1$.[10] A threshold $B_i(t)$, which varies with the number of iterations, is added to the iteration equation (2) for the state of the neuron:

$$S_i(t+1) = \text{Sgn}\left[\sum_{j \neq i}^{N} J'(i, j)S_j(t) - B_i(t)\right], \quad (10)$$

where

$$B_i(t) = \sum_{j \neq i}^{N} S_j(t)_o \quad (11)$$

Gardner and Derrida[7] with the replica method that the spin state corresponding to $P_{wi}[J(i,j)] = 0$ for a spin system unordered set: $J(i,j)$ with a distribution function (9) is unstable. In this work, we could not find a stable state that satisfies $P_{wi} = 0$ by Monte Carlo calculation using a random spin state as its initial state. This is in agreement with the conclusion drawn in reference 7. Nevertheless, the results of this study showed that when using unordered set: $J(i,j)$ given by (4) as the initial state, it is possible to obtain a stable state unordered set: $J^*(i,j)$ that corresponds to $P_{wi} = 0$.

The Monte Carlo learning algorithm presented in this work can also be used to optimize other neural networks.

References

1. J. J. Hopfield, Proc. Natl. Acad. Sci. USA, 1982, 79, 2554.

2. Wang Baohan [3679 1405 5060], SHENGWU WULI XUEBAO [CHINESE JOURNAL OF BIOPHYSICS], 1989, 5, 89.

3. W. Kinzel, Z. Phys., B-Condensed Matter, 1985, 60, 205.

4. D. Psaltis and N. H. Farhat, Optics Letters, 1985, 10, 98.

5. J. L. Van Hemman, D. Grensing, A. Huber and R. Kuhn, J. Stat. Phys., 1988, 50, 259.

6. D. J. Amit and H. Gutfreund, Ann. Phys., 1987, 173, 30.

7. E. Gardner and B. Derrida, Ann. Phys. (A): Math. Gen., 1988, 21, 271.

8. Chen Tianlun, Huang Wuqun, and Zheng Xite [6774 1585 3676], GAONENG WULI YU HEWULI [HIGH ENERGY PHYSICS AND NUCLEAR PHYSICS], 1985, 9, 41. Chen Tianlun, Huang Wuqun, Jin Ke [6855 2688], and Suo Cunchuan [4792 1317 1557], GAONENG WULI YU HEWULI, 1989, 13, 188. Ke Jin, Chen Tianlun, and Huang Wuqun, J. Phys. (A): Math. Gen., 1989, 22, 4179.

9. N. Metropolis et al., J. Chem. Phys., 1953, 21, 1087.

10. N. H. Farhat et al., "1986, in Neural Networks for Computing, Ed. J. Penkar," (Amer. Inst. Phys., New York), 146-152.

Fluorophosphate Glass for High-Power Laser System

[Article by Jiang Yasi [5592 0068 4828], Zhang Junzhou [1728 0193 3166], Xu Wenjuan [6079 2429 1227], Mao Hanfen [3029 3211 5358], and Ying Xiongxin [2019 7160 0207] of Shanghai Institute of Optics and Fine Mechanics of the Chinese Academy of Sciences: "Fluorophosphate Glass for High-Power Laser System"]

[Text] **Abstract**

Based on a study of the effect of each constituent on the spectral and physical characteristics of the glass, a practical glass composition and the associated technology were determined in this work. The only remaining problem is impurity in the glass which is being resolved.

Key words: Neodymium, laser, fluorophosphate glass, high-power laser system, stimulated emission cross-section.

I. Introduction

Advances in glass technology have been made due to requirements of high power laser systems on glass materials. The research on fluorophosphate glass began in 1940. In 1961, optical fluorophosphate glass numbers began to appear.[1] In the early stage of laser glass development when we were searching for new excitable ions and suitable substrates, as well as in later studies,[2,3] the characteristics of Nd^{3+} in fluorophosphate glass have been investigated. It was also found to lase upon excitation in fluoro-beryllate glass.[4] However, fluorophosphate glass was not considered as a practical laser glass substrate back then.

The development of fluorophosphate glass came about with high power lasers. Due to non-linear effect, self-focusing limits further increase in the power density of the laser. Lowering n_2 has become one of the major requirements of a high power laser system on the glass material. Table 1 shows the figures of merit of all glass elements in a laser, including transmitting and excitation elements. As far as the merit figures are concerned, fluorophosphate glass is suitable for transmitting elements (such as lens, window, polarized substrate), stimulation element (working medium) and even the dielectric medium in a Faraday magnetic-optical isolator.

Table 1. Relative Figures of Merit for the Optical Glasses

Component	Fig. of merit	Silicate glass	Phosphate glass	Fluorophosphate glass	Fluoro-beryllate glass
Laser disk (at Brewster's angle)	n^2/n_2	1.0	1.4	2.3	3.1
Window	n/n_2	1.0	1.4	2.3	3.6
Lens	$n(n-1)n_2$	1.0	1.3	2.0	2.2

As an amplifying medium, the gain is dependent upon the excited cross-section σ. The optimal σ depends on the operating condition of the laser. A short-pulse unsaturated-gain laser amplifier requires a high σ material in order to attain the maximum gain. Excessively high σ causes the parasitic resonance of a large aperture laser disk to increase to destroy its amplifying property. Different glass should be selected for each laser system based on its characteristics.
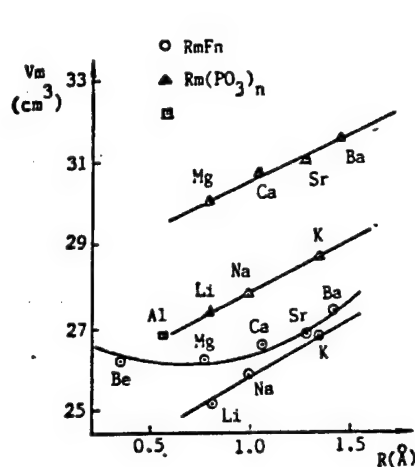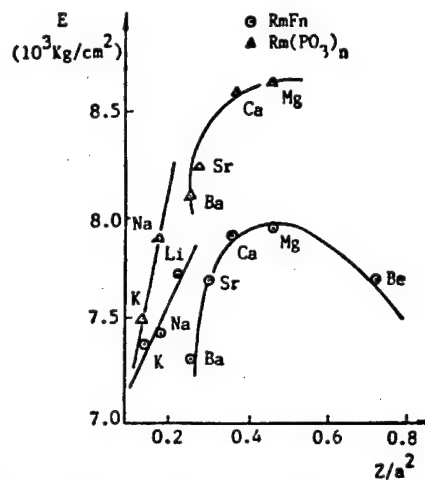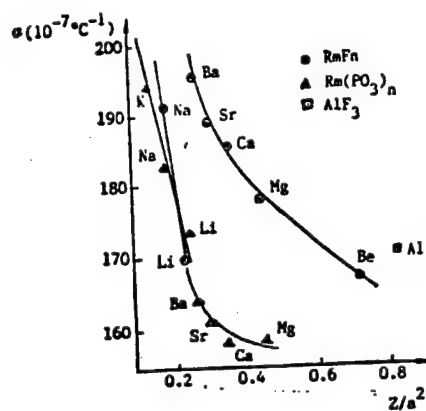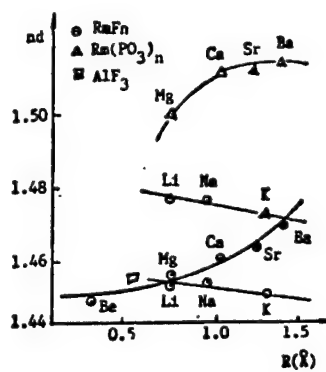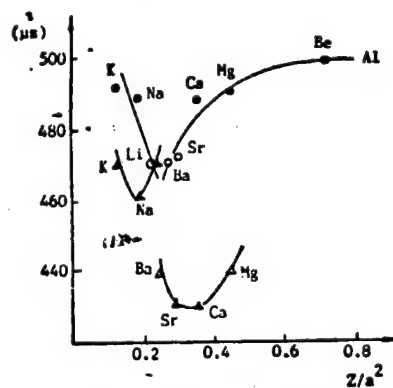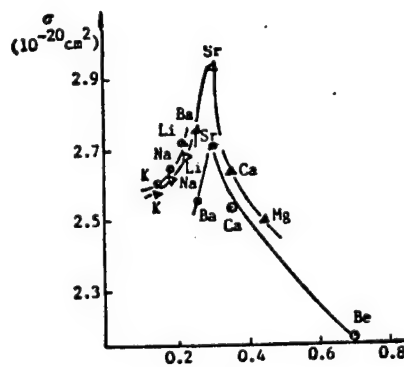
Reports and product literature regarding Nd-doped fluorophosphate glass began to appear after 1977.[5-11] The characteristics of various fluorophosphate glasses do not differ by much. However, further improvements in areas ranging from performance testing to technical specifications are needed. Prior to 1976, Lawrence Livermore National Laboratories was considering whether phosphate glass or fluorophosphate glass was to be developed as the new working medium for the new laser system under construction.[12] Several years later, it was believed that phosphate glass has its limitations as a large diameter laser disk. Therefore, fluorophosphate glass was given priority as the working medium for the 200-300 TW NOVA system.[13]

Since 1977, Shanghai Institute of Optics and Fine Mechanics began to investigate fluorophosphate laser glass on the basis of its existing work on fluorophosphate optical glass. The work covers areas such as synthesis of raw materials, physicochemical properties of glass, glass composition, special melting technology, waste treatment and testing of laser characteristics. In 1981, laser in fluorophosphate glass was achieved.[14] This paper summarizes the results in glass composition and glass types.

II. Effect of Fluorophosphate Glass Composition on Its Characteristics

In a series of glasses containing: 18 MgF_2 x 18 CaF_2 x 8 SrF_2 x 10 BaF_2 x 22.5 AlF_3 x 13.5 $NaPO_3$ (mol%), an additional 10 mol% of a variety of fluorides or metaphosphates was added to maintain the Nd^{3+} content at 1 x 10^{20} cm^{-3}. The physicochemical properties and other laser-related characteristics were measured and shown in Figures 1-6.

From the figures, the effect of cation on the glass properties is similar to those for silicate and phosphate glass. Molecular volume increases with increasing cation

32 LASERS, SENSORS, OPTICS

Fig. 1   Molecular volume V_m vs cation radius

Fig. 2   Young's modulus E vs Z/a^2

Fig. 3   Linear thermal expansion coefficient vs Z/a^2

Fig. 4   Refractive index vs cation radius R

Fig. 5   Fluorescence lifetime of Nd^{3+} vs Z/a^2

Fig. 6   Stimulated emission cross section of Nd^1 at 1.05 μm vs Z/a^2

radius. Elastic modulus E and thermal expansion coefficient are determined by the attractive force between cation and anion, expressed in terms of Z/a^2 where Z is the valence of the cation and a is the distance between the cation and the fluoride ion. Index of refraction also varies with increasing cation radius in the same manner as in phosphate or silicate glass. However, a comparison of glasses with same mol% of metaphosphate and fluoride, the presence of fluoride loosens the glass structure. It causes the molecular volume to increase, elastic modulus to drop and thermal expansion coefficient to rise. Fixed by the Be^{2+} to anion radius ratio, it is easy to form a $[BeF_4]^{2-}$ tetrahedral cluster in fluorophosphate glass which becomes a part of the phosphorus-oxygen-fluorine and aluminum-oxygen-fluorine tetrahedrons in the glass network. Similar to what happens in crystalline minerals, an increase in structural gap also makes the molecular volume go up and a decrease in valence causes the elastic modulus to go down. Similar trends can be found with Mg^{2+} because of its small radius.

The fluorescent line width of Nd^{3+} in fluorophosphate glass is relatively wide. In commercially available laser glasses, the half widths at 1.05 µm of phosphate glasses LHG_5, LHG_7 and LHG_8 manufactured by HOYA in Japan are about 18.0-20.1 nm at room temperature. For fluorophosphate glass LHG_{10}, it is 24.1 nm.[11] In this work, we also observed the broadening of Nd^{3+} fluorescence. It might be due to different emitting centers in Nd^{3+}. Different from silicate and phosphate glasses, fluorophosphate glass simultaneously contains oxygen and fluorine anions. In the system studied, the F^- to O^{2-} ratio is approximately 4:1. Nd^{3+} could be incorporated in an oxygen, fluorine-oxygen polygon or fluorine polyhedron. In addition to line broadening in the system studied, it was obvious there are two fluorescent peak wavelengths λ_p at 1.052 µm and 1.055 µm, respectively.

These two wavelengths correspond to

λ_p = 1.052 µm, LiF, BeF_2, MgF_2, CaF_2, AlF_3;

λ_p = 1.055 µm, NaF, KF, SrF_2, $Rm(PO_3)_n$.

It is believed that λ_p = 1.055 µm belongs to Nd^{3+} emitting from an oxygen coordination system. The peak wavelength is identical to that in phosphate glass. λ = 1.052 µm corresponds to a Nd^{3+} emitting center in an oxygen-fluorine coordination system. Increasing the metaphosphate content makes the emitting center move toward the oxygen coordination mode. Introducing a fluoride of small ionic radius or capable of forming a framework in the glass makes it easy for Nd^{3+} to be located at an oxygen-fluorine coordination center. Various Nd^{3+} emitting centers have their own fluorescence lifetimes and line widths. The measured results reflect the overall outcome. The stimulated emission cross section of Nd^{3+} at 1.052-1.055 µm is determined by the absorption cross section and fluorescent line width of each center. This makes the analysis more difficult.

Figures 5 and 6 are results of fluorescent lifetime and stimulated emission cross section measurements.

III. Fluorophosphate Glass Types

Selection of glass composition must simultaneously consider the effect of various fluorides on stimulated emission cross section, fluorescent lifetime, n_2 and other optical and physical characteristics. Similar to optical fluorophosphate glasses, three metaphosphate systems, i.e., $Al(PO_3)_3$, $Ba(PO_3)_2$ and $NaPO_3$, may be introduced. In optical fluorophosphate glasses developed in recent years, most of them use the $Al(PO_3)_3$ system in order to obtain glasses with less vitreous forming bodies, low index of refraction and high Abbe value.[15-17] In view of the research done on the composition and technology involving $NaPO_3$, we are still working on the $NaPO_3$ fluorophosphate glass system.

Table 2 lists the spectral, optical and other physical characteristics of the fluorophosphate glass developed. Most data were measured at Lawrence Livermore National Laboratories. Comparing to results of LHG_{10} of Hoya, Schott and LG_{810} of American Optical Co., the glass developed in our laboratory has higher stimulated emission cross section and thermal optical stability and lower temperature coefficient of optical path length. Figure 7 shows the concentration quenching curve of Nd^{3+} lifetime. When the doping level of Nd_2O_3 is more than 3(wt)%, its fluorescent lifetime declines. Laser glass was prepared by melting the ingredients in a crucible under a dry protective atmosphere. After annealing, it was ground into a 6-mm diameter 100-mm long laser rod. Tests showed that it has a higher gain and laser efficiency compared to Nd silicate glass.

Table 2. Properties of Fluorophosphate Laser Glass

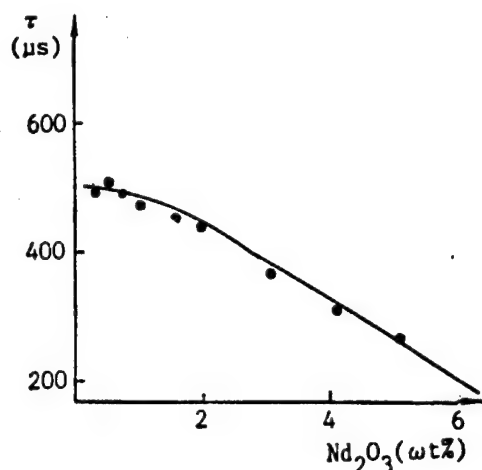|	
Nd_2O_3 (wt%)	2.0
Stimulated emission cross section (10^{-20} cm^2)	2.84
Fluorescence lifetime (µs)	405
Principle fluorescence peak (nm)	1053
Principle fluorescence peak line width (FWHM) (nm)	26.2
Attenuation coefficient at lasing wavelength (cm^{-1})	< 3
n_D	1.480
Abbe value	83.9
Non-linear refractive index n_2 (10^{-13} esu)	0.686
Temperature coefficient of refractive index dn/dt (10^{-7}°C^{-1})	-79
Coefficient of linear thermal expansion (10^{-7}°C^{-1})	157
Temperature coefficient of optical path length (10^{-7}°C^{-1})	-10
Transformation temperature T_g (°C)	420
Softening point T_f (°C)	465
Density (g/cm^3)	3.52
Young's modulus E (10^3N/mm^2)	80.9
Poisson's ratio µ	0.28

Figure 7. Concentration Quenching of Nd^{3+}-Fluorescence in Fluorophosphate Glass

IV. Laser Damage to Fluorophosphate Glass

Solid inclusions were found in fluorophosphate glass a long time ago. It is not an issue when used as an optical imaging material. At 4 J/cm^2 (1 ns), laser damage was found in the fluorophosphate glass. Furthermore, it was estimated that solid inclusions ranged from 10^6-10^7 piece/cm^3.

Optical microscopy and scanning electron microscopy have been used to analyze solid inclusions in fluorophosphate glass. Moreover, techniques such as X-ray spectroscopy, electron probe, micro and ultra-micro chemical analysis have been used to determine the composition of those solid inclusions.[18] The platinum contents in various fluorophosphate glass samples prepared under different conditions were determined. Under normal conditions, it contains approximately 10^{-8} of platinum. Electron probe micro-analysis from scattering points in the glass also detected X-ray spectrum characteristic to platinum. A combination of X-ray energy spectrum and scanning electron microscopy was used to analyze the impurity region. Precipitation of transition elements and silicon impurity was discovered. Under a polarized microscope, solid inclusions ranging from 10^5-10^6 piece/cm^3 have been found in all optical and laser fluorophosphate glasses made either domestically or abroad. They are present as polycrystalline micro-particles or vitreous products of metaphosphate or fluoride or high refractive index precipitates of oxides and heavy metal elements from hydrolysis and oxidation of fluoride. We believe these solid inclusions form destruction centers.

A 20 ns pulsed single mode focusing laser beam at 1.06 μm was used to determine the laser damage threshold of several fluorophosphate glasses. It is approximately 5 x 10^9 W/cm^2, which is only one-fourth of that of the Nd

silicate glass. It is consistent with what was reported in the literature.[19] Every country is working on reduction of solid inclusions and raising the damage threshold. However, it is still below 10 J/cm^2 (1 ns).

V. Conclusions

The fluorophosphate glass developed in this work has a small n_2 and high figure of merit. It has the appropriate stimulated emission cross section and fluorescent lifetime either as an excitation medium or the transmission material and magnetic-optical glass substrate in a laser. The laser wavelength of Nd^{3+} in a fluorophosphate glass differs very little from that in a phosphate glass. There is a possibility that they may be mixed in use. As the working medium of a large diameter disk, fluorophosphate glass can achieve the maximum gain for the entire system. The only problem is laser damage. After years of efforts, it is still unresolved. It is still being worked on at various laboratories and manufacturing facilities.

References

1. W. Jahn, Glastech. Ber. 1961, 34, No 1 (Jan), 197.

2. Yu Fuxi [0060 4395 3556], et al., KEXUE TONGBAO [SCIENCE], 1963, No 9 (Sep), 50; 1963, No 12 (Dec), 41.

3. V.P. Kolebkov, Physics and Chemistry of Glass, 1977, 5, No 3 (Mar), 249.

4. G. T. Petrovski, et al., Opt. Spectrosc., 1960, 21, No 1 (Jan), 72.

5. O. Doutschbein, Appl. Optics, 1978, 17, No 14 (Jul), 2228-2232.

6. "Schott Information" (3/77, Jener Glasswerk, 1977).

7. Laser Focus, 1977, 13, No 8 (Aug), 54.

8. Kunio Yoshida, "Laser Research", 1977, 5, No 3 (Dec), 209-216

9. "Schott Catalogue," (7510e, 1977).

10. "Owens-Illionis Catalogue," 1977.

11. "Hoya Glasses for High-Power Laser System," 1982.

12. D. Milam, M. J. Weber, IEEE. J. Quant. Elect., 1976, QE-12, No 8 (Aug), 512-513; 2-147-153.

13. "Laser Program Annual Report," (UCRL-50021-79, LLNL, 1980), 2-74-76.

14. Jiang Yasi, et al., First Chinese National Optical Glass Conference (Guilin, Guangxi, PRC, 1981).

15. Gan Fuxi, et al., J. Non-Crys. Solids, 1982, 52, No 1-3 (Dec), 263-273.

16. Jiang Yasi, et al., J. de Physique, 1982, No C9 (Dec), 315.

17. S. E. Stokowski, et al., J. Non-Crys. Solids, 1980, 40, No 1-3 (Jul), 481-487.

18. Zhuo Xiaoshui [0587 2400 3055], et al., ZHONGGUO JIGUANG [CHINESE LASERS], 1983, 10, No 10 (Oct), 726-729.

19. T. Izimitani, Y. Asahara, Electro-Opt/Laser Intl., (UK, 1980), 172-179.

Inner Mongolia Plans Optical Cable Project

*SK1310020590 Hohhot Inner Mongolia Regional
Service in Mandarin 1100 GMT 9 Oct 90*

[Text] The autonomous region began on 5 October to
build its first optical cable digital telecommunications
line between the cities of Hohhot and Baotou. The
construction of the 184-kilometer-long optical cable dig-
ital telecommunications line in the autonomous region
was designed by the Ministry of Posts and Telecommu-
nications. The equipment used in the project was
imported from France, the United States, and Japan,
respectively. The optical cable telecommunications
project will be completed and put into operation in June
1991.

Status Report of On-Line Isotope Separator in Lanzhou

[Article by Huang Yecheng [7806 2814 2052], Wang Tongqing [3769 0681 1987], Tan Jinfeng [6151 6930 1409], Guo Bin [6753 2430], and Fan Hongmei [5400 4767 2734] of the Institute of Modern Physics, Chinese Academy of Science, Lanzhou: "ISOLAN - the On-Line Isotope Separator in Lanzhou"]

[Text] Abstract

This paper describes the design principle, structure and characteristics of the on-line isotope separator ISOLAN. Off-line test results with Ar and Xe showed a resolution power of 700-1200. ISOLAN will be connected to the Lanzhou heavy-ion accelerator to conduct research on the synthesis of new nuclides from medium-energy heavy-ion nuclear reactions and nuclides far away from the stability line.

I. Introduction

On-line isotope separators are usually connected to a high-energy proton beam, reactor neutron beam, or low-energy heavy-ion beam. ISOLAN (ISOL in Lanzhou) serves as a terminal of a heavy-ion accelerator HIRFL. It operates on the medium energy (20-100 MeV/A) heavy-ion beam. This provides a very favorable condition for studying short-lived nuclides.

Medium-energy heavy-ion fragmentation reaction (projectile fragmentation) is the best way to produce low-mass neutron-rich and neutron-poor nuclides. It involves very little momentum transfer between the projectile and the target. The product has a velocity similar to that of the projectile and the angular distribution peaks near 0°. The isotope distribution of the fragment is a function of N/Z of the projectile and target. The more neutron-rich the projectile (or target nucleus), the more neutron-rich the fragment is and vice versa. Therefore, it is possible to obtain the desired nuclide by consciously selecting the projectile and target nucleus. A competing reaction mechanism, involving a few nuclear transfer processes between the projectile and target nucleus, against projectile fragmentation can yield neutron-poor or neutron-rich nuclides depending upon N/Z of the projectile. This is an effective way to yield a nuclide not too far away from the projectile. Based on these two reaction mechanisms, we have reached proton droplet line at Z = 23, 25, 27 and 29 and neutron droplet line at Z < 8. With a very heavy target nuclide, people also expect to detect a heavy nuclide having a proton number and Z close to those of the target.

Medium-mass products of a medium-energy heavy-ion reaction are results from competing reactions of spallation and fission. Fission produces neutron-rich nuclides. However, spallation yields a wide range of products scattered over neutron-poor and neutron-rich regions. The ratio of fission in the entire process depends on the potential energy of fission.

In order to study a variety of reaction mechanisms and nuclides with different properties, the on-line isotope separator is required to have high resolution and high separation efficiency. Therefore, the beam optics must be delicately designed. It was for this purpose that we improved the beam optics of the ISOLDE separator. The target ion source is an important part of an on-line separator. People have designed thick targets, multi-layer targets and ion targets with a helium jet to meet various experimental needs. In addition, people have attempted to build high-temperature targets and molten targets in order to explore the feasibility of synthesizing new nuclides that are resistant to high temperature. As the reaction mechanism associated with medium-energy heavy ions is studied in more detail and the target ion source technology advances further, we can expect that ISOLAN will play an important role in research and development in this area.

II. Beam Optical Principle

Because of advantages such as simple structure, compactness, ease of construction, low cost, high resolution and excellent performance of the ISOLDE (55° magnet)[1] separator, it was chosen as our design model.

The focusing principle of the 55° magnet is that charged particles enter the magnetic field as a parallel beam under the influence of a single lens and form an image at square root of 2R from the exit of the magnet by double focusing.

Based on transmission theory for charged particles:[2,3]

$$\sigma (Z) = M\sigma (O) M^T \quad (1)$$

where $\sigma(Z)$ and $\sigma(O)$ are the space matrices of charged particles at Z and O, respectively. M and M^T are the transmission matrix of the optical elements and its conjugate matrix, respectively. The optical path of the ISOLDE on-line isotope separator is shown in Figure 1 [not reproduced].

Let us assume that the initial state of a charged particle in the ion source is $(x_0, \theta_0]$ where x_0 is the maximum displacement and θ_0 is the maximum divergence angle. From Figure 1 we can see that charged particles going through the lens form a parallel beam. It is represented by $[x_1, \theta_1]$. This state might be considered as the object waist of the 55° deflecting magnet. The waist-forming characteristics of charged particles can be studied using the transformation shown in equation (1).

Assume the waist state is [x, θ]. On the horizontal plane we have

$$\begin{bmatrix} x \\ \theta \end{bmatrix} = \begin{bmatrix} 1 & l_{2H} \\ 0 & 1 \end{bmatrix}\begin{bmatrix} a_{11} & a_{12} \\ a_{21} & a_{22} \end{bmatrix}\begin{bmatrix} 1 & l_1 \\ 0 & 1 \end{bmatrix}\begin{bmatrix} x_1 \\ \theta_1 \end{bmatrix} = H\begin{bmatrix} x_1 \\ \theta_1 \end{bmatrix} \qquad (2)$$

where l_1 is the object distance of the magnet, l_{2H} is the image distance on the horizontal plane, $a_{ij}(i, j = 1, 2)$ are the matrix elements of the magnet on the horizontal plane, and H is the new matrix transformed from equation (2). Since

$$\sigma = H\sigma_1 H^T \qquad (3)$$

therefore

$$\begin{bmatrix} \sigma_{11} & \sigma_{12} \\ \sigma_{21} & \sigma_{22} \end{bmatrix} = H\begin{bmatrix} x_1^2 & 0 \\ 0 & \theta_1^2 \end{bmatrix}H^T. \qquad (4)$$

The envelope equation and maximum divergence angle in the horizontal direction are

$$x_{max} = \sqrt{\sigma_{11}}, \qquad (5)$$

$$\theta_{max} = \sqrt{\sigma_{22}}, \qquad (6)$$

The extreme values of θ and x corresponding to the image waist θ_{min} and x_{min} are

$$\theta_{min} = \sqrt{\sigma_{22}} = \sqrt{H_{21}^2 x_1^2 + H_{22}^2 \theta_1^2} =$$

$$H_{21}x_1 = \frac{\cos\alpha}{l_{2H}} x_1, \qquad (7)$$

(when $\theta_1^2 \to 0$, for a parallel beam)

$$x_{min} = \frac{E}{\pi\theta_{min}} = \frac{l_{2H}E}{\pi x_1 \cos\alpha}, \qquad (8)$$

where $H_{ij}(i, j = 1, 2)$ are elements of matrix H.

Hence, the resolution is

$$R . P = \pi Dx_1 \cos\alpha / l_{2H}E, \qquad (9)$$

where D is dispersion.

When the emissivity E of the ion source remains unchanged, the only way to raise resolution power is to increase the width x_1 of the parallel ion beam before entering the magnet.[4-6] Technically, the best way is to install a quadrupole lens in front of the magnet. ISOLAN was designed according to this scheme. Its beam envelope is shown in Figure 2 [not reproduced].

III. ISOLAN Layout

Figure 3 shows a layout of the HIRFL building in Lanzhou. R_1 on the lower left is ISOLAN. The heavy-ion beam from HIRFL bombards the ISOLAN target ion source to initiate nuclear reactions. Products are captured, re-released, ionized and accelerated in the ion source. Under the influence of the single lens and quadrupole lens, charged particles form a wide parallel beam to pass through the magnet for mass spectrometric analysis. It forms a double waist (double focusing) at the reception chamber. In order to meet different experimental needs, the beam is controlled by switching codes to transport the mass-separated ion beam to a point 4 meters away. It is re-focused by a triple quadrupole lens assembly. As for the other three branch beams (see Figure 4), one is used for the study of new nuclide synthesis and new decay models on a transport system and the appropriate detectors. The second branch is equipped with a laser spectrophotometer to measure nuclear spin, magnetic moment, electric quadrupole and mean square radius change of charge of short-lived nuclides. The third branch can collect radioactive specimens for off-line analysis. Or, it can be equipped with a high-resolution mass spectrometer to conduct direct measurement of nuclear mass in order to extract information on nuclear structure far away from the stability line.
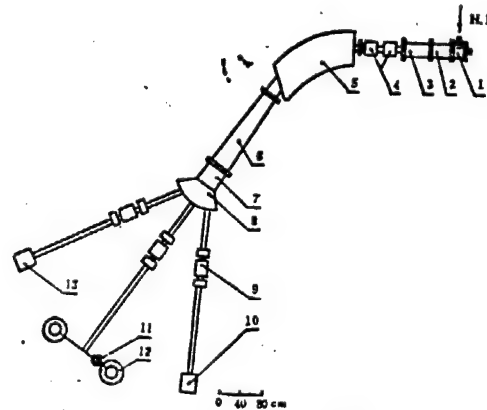

Figure 4. Layout of ISOLAN

Key: 1. target - ion source 2. single lens chamber 3. X, Y deflection plates 4. quadrupole lens 5. 55 ° magnet 6. dispersion chamber 7. target chamber 8. beam switch 9. quadrupole lens 10. radioactive specimen receptacle 11. detector 12. belt conveyor 13. delayed particle decay study, or laser spectrophotometer, mass spectrometer
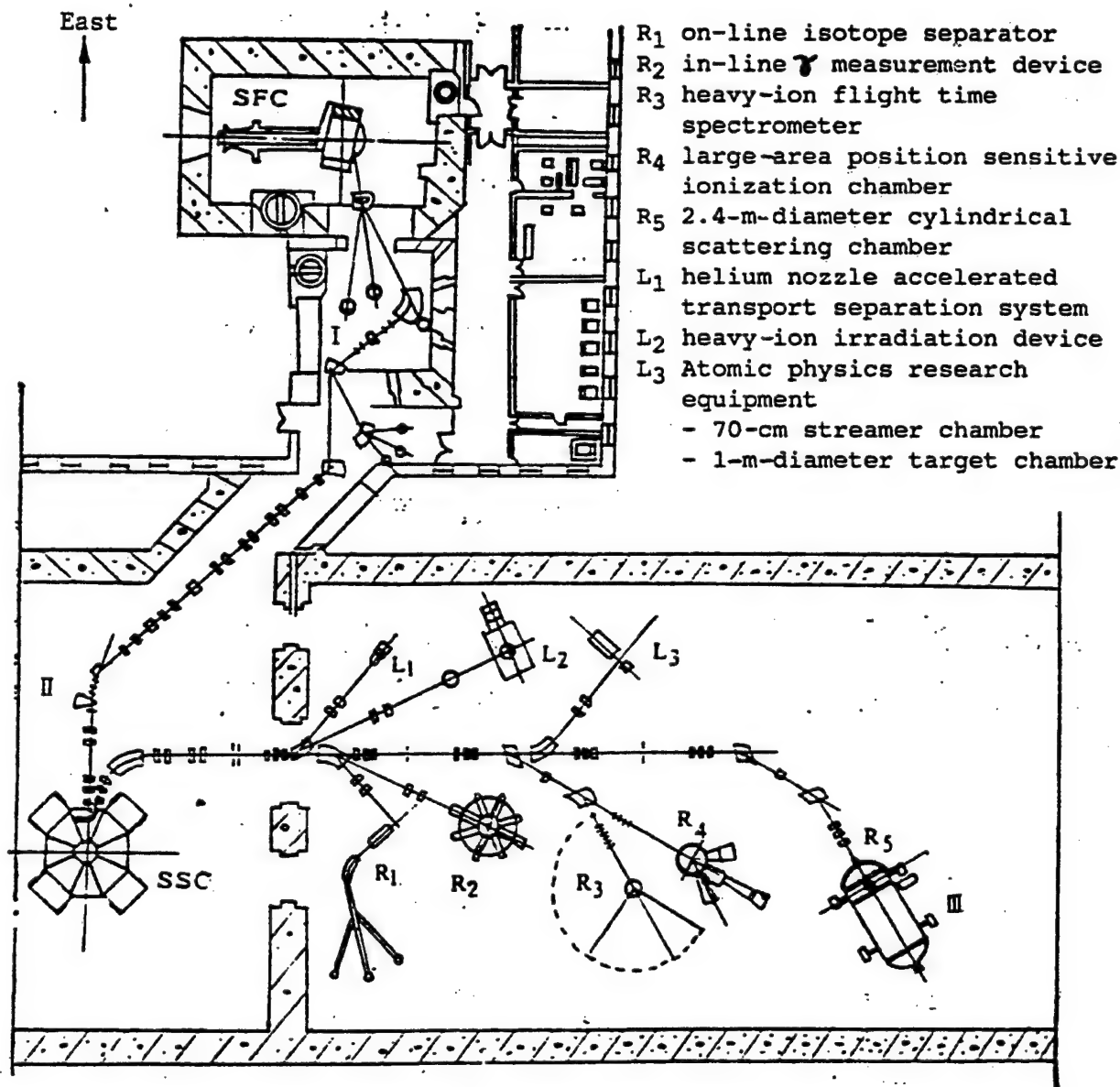
Figure 3. Layout of the HIRFL Floor Plan

East

SFC

R₁ on-line isotope separator
R₂ in-line γ measurement device
R₃ heavy-ion flight time spectrometer
R₄ large-area position sensitive ionization chamber
R₅ 2.4-m-diameter cylindrical scattering chamber
L₁ helium nozzle accelerated transport separation system
L₂ heavy-ion irradiation device
L₃ Atomic physics research equipment
 - 70-cm streamer chamber
 - 1-m-diameter target chamber

IV. Details of ISOLAN

1. Magnet[7]

This is a 1.5-m-radius, 54.7° deflection angle, "H"-shaped homogeneous field magnet. Its gap and pole width are 6 cm and 22 cm, respectively. The magnetic field strength is 4000 gauss and the maximum separable mass is 250. Over an 80 mm width range, the uniformity of the magnetic field is better than 1.4×10^{-4}. This meets the high-resolution design requirement. The magnet weighs approximately 1 ton and is compact and flexible.

2. Vacuum System

To minimize degassing, the chamber is made of stainless steel. There are four 300 liters/sec oil diffusion pumps evenly distributed in the main unit. Two are located in the ion source chamber and quadrupole lens chamber. The other two are located near the dispersion chamber and receiving chamber to ensure excellent vacuum in all areas in order to minimize scattering and charge transfer between ions and neutral particles. It was found experimentally that when the gas-intake rate of the ion source is 5×10^{-4} torr-liters/sec, the ion source has a vacuum of 0.8 to 1.3×10^{-5} torr and the receiving chamber has a vacuum of $3.0 - 5.0 \times 10^{-6}$ torr. Thus, ion-beam focusing conditions are completely met.

3. High-Voltage Power Supply and Magnetic Field Power Supply

The total width of the ion beam from the ion source through the analyzer to the receiving chamber is:[8]

$$W_T = R \frac{dV}{V} + 2R \frac{dB}{B} + S_0 + p, \qquad (10)$$

where R is the radius of the magnet. The first term is contributed by the instability of the accelerating magnetic field. The second term is due to the instability of the magnetic field. The third term represents the magnitude of the pseudo source, usually $S_0 < 1$ mm. The fourth term is the aberration of the magnet. For parallel beam incidence, $\theta_1 \approx 0°$, therefore $p \approx 0$. Hence, the size of the focusing spot is primarily determined by the stability of the electric and magnetic fields. The ripple and stability of the high-voltage power supply is 1.6 x 10^{-4} and that of the power supply for the magnetic field is 1.0 x 10^{-4}. They both meet design requirements.

4. Ion Source

Off-line tests were done with a hollow cathode ion source.[9] Its characteristics include compactness, large electron emission surface, and excellent heat shielding. It is capable of improving ionization efficiency. The gas-intake rate of the ion source is approximately 5 x 10^{-4} torr-liters/sec. With the right parameters, when the arc chamber temperature is between 950 and 1100°C, the ion source can operate stably over extended periods of time. In future on-line work, a FEBIAD source[10] will be used to satisfy the needs of a wider variety of experiments.

V. Off-Line Test Results

Table 1 shows the technical specifications for ISOLAN. In off-line tests, because of using a three-electrode exit system and a strongly focusing triple-cylinder lens (see Figure 5 [not reproduced]), the beam extracted is relatively divergent. Under the influence of the strongly focusing lens, it forms a wide parallel beam to enter the magnetic field. Hence, even under the circumstance that the two quadrupole lenses are not yet installed, very high resolution was achieved. Tests with respect to Ar and Xe show that the resolution power is 700-1200. Figure 6 [not reproduced] shows the X, Y recorder plot of a Xe isotope mass spectrum detected by a scanning probe (0.5 mm diameter) at the focal plane of the receiving chamber.

Table 1. Technical Specifications of ISOLAN

Deflection angle of magnet α	54.7°
Radius of magnet R	150 cm
Magnetic field strength B	4000 gauss
Magnetic field uniformity	< 1.4 x 10^{-4}
Accelerating voltage V	50 kV

Separable mass number	250
Simultaneously receivable mass number	100 plus or minus 10
Resolution power (with quadrupole lens) R.P	1000 - 1500
Resolution power (without quadrupole lens) R.P	700 - 1200
Separation efficiency η	10^{-4} - 10^{-2}
Dispersion D	7.5 mm at mass number 200

Success in off-line tests signified the completion of ISOLAN. It will be available for nuclear physics research.

References

1. A. Kjelberg and G. Rudstam, CERN 70-3.

2. K. L. Brown, SLAC-75.

3. K. L. Brown, SLAC-91.

4. Huang Yecheng, NUCL. INSTR. AND METH., B26(1987), 25.

5. H. Wollnik, NUCL. INSTR. AND METH., 95(1971), 453.

6. B. R. Nielson, NUCL. INSTR. AND METH., 186(1981), 457.

7. Wang Tongqing and Guo Bin, HE WULI DONGTAI [STATUS OF NUCLEAR PHYSICS], 2(1980), 50.

8. J. H. Freeman, "Ion Implantation," 1973, p 389.

9. Tan Jinfeng, Symposium of the Third Chinese National Conference on Ion Sources, September 1987, Lanzhou.

10. R. Kirchner, et al., NUCL. INSTR. AND METH., 186(1981), 295-305.

Acceleration Effect on Separation of Uranium Isotopes Studied

[Article by Zhu Guangming [2612 0342 2494] and Qiu Ling [6726 7117] of Lanzhou University and Lu Xianyao [7120 7359 1031] of Beijing Institute of Nuclear Chemical Engineering and Metallurgy: "Study on the Application of Acceleration Effect to Separation of Uranium Isotopes by Cation Exchange"]

[Text] **Abstract**

This paper studies the acceleration effect of succinic acid and Ca^{2+} on the separation of uranium isotopes of the UO_2^{2+}-malic acid-Na^+ displacement system. The chromatographic characteristics, single-stage separation factor ε of uranium isotopes, slope coefficient g and the temperature coefficients of the UO_2^{2+}-Mal-Suc-$Ca^{2+}(NH_4^+)$ displacement system have been determined and compared to those of the UO_2^{2+}-Mal-Suc-$Ca^{2+}(Na^+)$ displacement system. It confirms that the acceleration effect of Ca^{2+} on the mass transfer of UO_2^{2+} causes g to increase by 63 percent, or ε x g to go up by 37 percent. It also illustrates that the pH in the uranium plateau of the UO_2^{2+}-Mal-Suc-$Ca^{2+}(NH_4^+)$ system is controllable. Therefore, it is adaptable for obtaining the optimal separation condition.

Key words: Separation of uranium isotopes, acceleration effect, cation exchange

I. Introduction

The authors[1-5] have reported the acceleration effect of percarboxylic acids and hydroxyl carboxylic acids and a series of metal ions on the separation of UO_2^{2+}.

Uranium isotope separation by ion exchange with U(IV)-U(VI) and UO_2^{2+}-UO_2L_x exchange systems has been in use for merely 30 years. Although the former system is believed to have a brighter prospect because of its large separation factor, however, the latter has certain technical advantages which keep its research going on for a long time. The key issue is to find an ideal reagent to boost the separation factor ε of the system to a sufficiently high level. Moreover, it has a fast isotope heteropical exchange rate (expressed in terms of slope factor g[6-7]). As for the former, Okamoto[8] recently reported that the UO_2^{2+}-Mal-Na^+ displacement system has the highest ε among all the systems investigated. As for the latter, based on the study of acceleration effect in references 1-5, it was known that the malic or succinic acid and Ca^{2+} have a significant acceleration effect on the mass transfer of UO_2^{2+}. Based on these results, the chromatographic characteristics of the UO_2^{2+}-Mal-Suc-$Ca^{2+}(Na^+$ or $NH_4^+)$ displacement system is studied in this work.

Major parameters of column separation of uranium isotopes ε and g and their temperature coefficients are determined. Compared to the UO_2^{2+}-Mal-Na^+ displacement, it has been confirmed that the acceleration effect of Suc + Ca^{2+} could raise the value of g by 63 percent. Despite a slight decline of ε, ε x g still increased by 37 percent. In addition, because pH is adjustable in the uranium plateau, this system offers more possibility for selecting a more optimal experimental condition.

II. Chromatographic Characteristics of UO_2-Mal-Suc-$Ca^{2+}(Na^+)$ Displacement System

1. Chromatographic Characteristics

As mentioned earlier, liquid-phase succinic acid and Ca^{2+} in the resin phase showed a significant acceleration effect on the UO_2^{2+} - H^+ exchange and the kinetics[4] for UO_2^{2+} - H^+ are similar to those of $^{235}UO_2^{2+}$ - $^{238}UO_2^{2+}$. Hence, the displacement system Mal-Suc-Ca^{2+} may accelerate the exchange between $^{235}UO_2^{2+}$ - $^{238}UO_2^{2+}$, i.e., changing the isotope exchange rate. However, it requires a large amount of mass spectrometer data to determine the acceleration effect directly from isotope column separation experiments. As a preliminary test, the steepness of the interface in the stable uranium plateau can be used to express the rate of $^{235}UO_2^{2+}$ - $^{238}UO_2^{2+}$ exchange. The steeper the interface is, the smaller the HETP [height equivalent to a theoretical plate], or the larger the g is in the separation process.

The stable interface equation can be expressed by the equilibrium column plate formula[9] under complete refluxing condition:

$$h/\lg\alpha_A^B = L_2^1 \Big/ \frac{(X_A/X_B)_1}{(X_A/X_B)_2} \quad (1)$$

In this study, the front interface is sufficiently steep. Therefore, h represents the equivalent column plate height at the rear interface where UO_2^{2+} is displaced based on Martin theory. α_A^B is the separation factor of the process and $h/\lg\alpha_A^B$ is a parameter expressing the steepness of the interface.

Another parameter used in the study of chromatographic characteristics is the pH at the uranium plateau (expressed as pH*). Since ε and g are related to the degree of complexing of UO_2^{2+} in the solution, therefore, they are dependent upon pH*. However, when a displacement reagent is made of a single complexing acid, pH can hardly be affected by varying the concentration of the complexing acid, or the pH of the displacement reagent (expressed as pH**). Hence, it is difficult to choose a separation condition. In view of the fact that succinic acid shows an acceleration effect on the mass transfer of UO_2^{2+} it also may serve as a buffer to raise the value of pH. This is just like adding NH_4Ac to EDTA in rare-earth separation. Therefore, it was chosen as a second component.

2. Experiment

Spherical porous polystyrene sulfonic-acid ion-exchange resin (No. 840209), 35-36 μm diameter when wet, 8 percent crosslinking, was packed in a column in saturated ammonium nitrate solution by free fall. The column is 9.5 mm in diameter and 600 mm long. It is equipped with a constant-temperature water jacket.

The Mal-Suc-$Ca^{2+}(Na^+)$ displacement reagent is prepared as follows:

Weigh out equimolar malic acid and succinic acid (A.R.). Add water to dissolve the acids and place it in a volumetric flask. Add a pre-determined amount of lime water and adjust its pH to a specific value with NaOH of known concentration. The exact concentration of Ca^{2+} was determined by back titration of Zn^{2+} with an excessive amount of EDTA. The molar ratio of malic acid to succinic [Mal]/[Suc] was chosen to be 1. The acceleration effect of succinic acid is most prominent at this ratio.

A peristaltic pump was used for fluid delivery with an H-shaped HNO_3 rotating rotor. Ten ml of 0.50 mol/l $UO_2(NO_3)_2$ was used. Displacement was carried out at a constant rate (V)*** of 1 cm/min. As it penetrates the uranium section, fluid was extracted at various positions. Uranium was measured by the NH_4VO_3 method and the pH distribution was determined with a pH meter.

3. Results

Table 1 shows the results of 12 rounds of displacement experiments. In the table, K_d is the molar ratio of uranium in solid phase to that in liquid phase; $K_d = [\overline{U}]/[U] = V^{***}/\overline{V} - \alpha_o$ and $\overline{V}$ is the moving rate of the stable uranium region, α_o is the void index of the column. K_d can be calculated from V^{***}, $\overline{V}$ and α_o.

Table 1. Chromatographic Parameters of $\overline{UO_2}^{2+}$-Mal-Na^+, $\overline{UO_2}^{2+}$-Mal-Suc-Na^+, and $\overline{UO_2}^{2+}$-Mal-Suc-$Ca^{2+}(Na^+)$ Displacement Systems (25°C, Highly Porous Sulfonic Ion Exchange Resin)

Number		1	2	3	4	5	6	7	8	9	10	11	12
Complexing acid, mol/l	[Mal]	0.200	0.100	0.100	0.100	0.100	0.100	0.100	0.100	0.100	0.100	0.120	0.130
	[Suc]	0	0.100	0.100	0.100	0.100	0.100	0.100	0.100	0.100	0.100	0.120	0.130
Displacement ion, mol/l	[Na^+]	0.378	0.350	0.281	0.400	0.333	0.242	0.194	0.289	0.236	0.198	0.319	0.340
	[Ca^{2+}]	0	0	0.380	0.020	0.0334	0.025	0.0180	0.0268	0.0562	0.0767	0.0304	0.0324
	[Ca^{2+}]/[Na^+]		0	0.135					0.0956	0.238	0.387	0.095	0.095
pH**		5.20	5.20	5.21	7.88	6.90	4.93	4.50	5.21	5.24	5.23	5.22	5.23
pH*		2.08	2.63	2.67	2.92	2.95	2.47	2.25	2.69	2.69	2.67	2.83	2.88
K_d		3.85	3.81	3.71	3.14	3.63	4.89	6.39	3.42	3.22	3.53	3.76	3.54
h/lgα, cm		1.04	0.69	0.47					0.54	0.79	1.27	0.95	1.11

A comparison of the results of experiments 1, 2 and 3 shows that:

(1) The addition of succinic acid and Ca^{2+} has little effect on the uranium distribution in the two phases. However, it could significantly increase pH* and lower h/lgα.

Comparing the results of experiments 4, 5, 3, 6 and 7 we found that:

(2) pH* dropped considerably with pH** and it would not be difficult to control pH** over the range 2.2-3.0.

Comparing the results of experiments 2, 8, 3, 9 and 10 we found that:

(3) At the same pH** and pH*, h/lgα declines to a minimum and then rises again with increasing Ca^{2+} content or Ca^{2+} to Na^+ ratio [Ca^{2+}]/[Na^+].

Comparing the results of experiments 8, 11 and 12 we found that:

(4) Increasing the concentration of malic acid and succinic acid could raise the value of h/lgα, which reduces the steepness of the trailing interface of uranium region.

Looking at the values of K_d in nos. 2-10, we also found that:

(5) Although the composition of the displacement reagent (concentration of complexing acid and displacement ion and pH) varies over a wide dynamic range, K_d only varies between 3.2 and 6.4. (The optimal K_d for chromatography is in the 3-6 range.)

From the above, using Mal-Suc-$Ca^{2+}(Na^+)$ as the displacement reagent can make the uranium interface steeper. It is possible to adjust the pH* in the uranium region and a suitable and steady K_d can be maintained.

The first two items indicate that the $^{235}UO_2^{2+}$ - $^{238}UO_2^{2+}$ exchange can be accelerated and that it may be possible to choose the acceleration condition. The last item is a premise to use displacement separation.

III. Using UO_2^{2+}-Mal-Suc-$Ca^{2+}(NH_4^+)$ Displacement Column for Uranium Isotope Separation

1. Experiment

A plexiglass column (10.6 mm diameter x 2,000 mm long) and glass column (8.26 mm diameter x 2,000 mm long, for higher temperature work) with constant-temperature water jacket were used. The same ion exchanger and column packing procedure as described earlier were used. A mechanical pump was used to pump fluid at a constant rate. The fluid was pre-heated by passing through a 3-mm-diameter x 2,000-mm-long stainless tube with a constant-temperature water jacket. The dead volume at the exit of the column was reduced to a minimum in order to prevent isotopes from mixing. The stable uranium region is approximately 12 cm in length. The same procedures as before were used for sample extraction, uranium analysis and pH measurement.

Uranium isotopes were analyzed as follows. Any Fe^{3+} in the sample was reduced to Fe^{2+} with ascorbic acid in 4 mol/l hydrochloric acid. It then passed through an anion-exchange column to adsorb uranyl-chloride anions. After removing organic acid impurities and Fe^{2+} and Ca^{2+} with 4 mol/l HCl, uranium was washed out with deionized water (pH < 2). It was baked dry under an infrared lamp. Nitric acid was added four times to convert it into uranyl nitrate. Afterward, it was made into a sample to be analyzed on a MAT-261 mass spectrometer (West German) for uranium isotope analysis.

2. Data Processing

The separation factor ε for a single-stage process is calculated based on the following equation:[9]

$$\varepsilon = \frac{\Sigma C_i V_i (R_i - R_o)}{q R_o (1 - R_o)} \qquad (2)$$

where R_o and R_i are the uranium isotope abundance of the raw material and that of the ith sample, respectively; V_i and C_i are the volume and molar concentration of uranium of the ith sample; q is the uranium molar concentration in the resin bed, which is $q = K_d$ x bed volume x molar concentration of uranium in the plateau.

The slope coefficient g can be calculated from the following equation.[8]

$$\frac{\Delta R\ (V,\ t)}{\Delta V} = g[R\ (V, t) - R_o + A'(t)\ ] \quad (3)$$

It is obtained by plotting. In this equation, R is the abundance of uranium isotope, which is a function of displacement time t and displacement distance or discharged fluid volume V. Since the region where ^{235}U is enriched is far narrower than the height of the bed, t can be considered constant. Therefore, $\Delta R/\Delta V$ can be found from the R(V)-V curve based on experimental data. Then, $\Delta R(V)/\Delta V$ can be plotted against R(V) to obtain a straight line, and its slope is equal to g.

3. Results

At 25°C, Mal-NH_4^+ (pH** 5.46), Mal-Suc-NH_4^+ (pH** 5.75), Mal-Suc-NH_4^+ (pH** 4.65), and Mal-Suc-$Ca^{2+}(NH_4^+)$ (pH** 5.53) were used as displacement reagents. Displacement experiments were carried out in Plexiglass columns at approximately the same flow rate. All experimental conditions and results are listed in Table 2. Figure 1 shows typical curves for R(V), pH and uranium concentration versus V.

Table 2. Experimental Conditions and Results of Uranium Isotope Separation With Four Displacement Reagents. Bed height 188 cm; column cross-section 0.88 cm²; R_o = 0.50; 25°C.

Complexing acid, mol/l	[Mal]	0.200	0.100	0.100	0.100
	[Suc]	0	0.100	0.100	0.100
Displacement ion, mol/l	[NH₄⁺]	0.384	0.384	0.256	0.288
	[Ca²⁺]	0	0	0	0.0400
pH**		5.46	5.75	4.65	5.53
pH*		2.08	2.92	2.40	2.70
V***, cm/min		1.00	0.90	0.93	0.91
∇, cm/min		0.27	0.23	0.16	0.24
K_d		3.58	3.84	6.01	4.02
Uranium plateau concentration, mol/l		0.190	0.200	0.130	0.201
ε x 10⁴		2.30	1.90	1.48	1.94
g, cm⁻¹		0.27	0.34	0.40	0.44

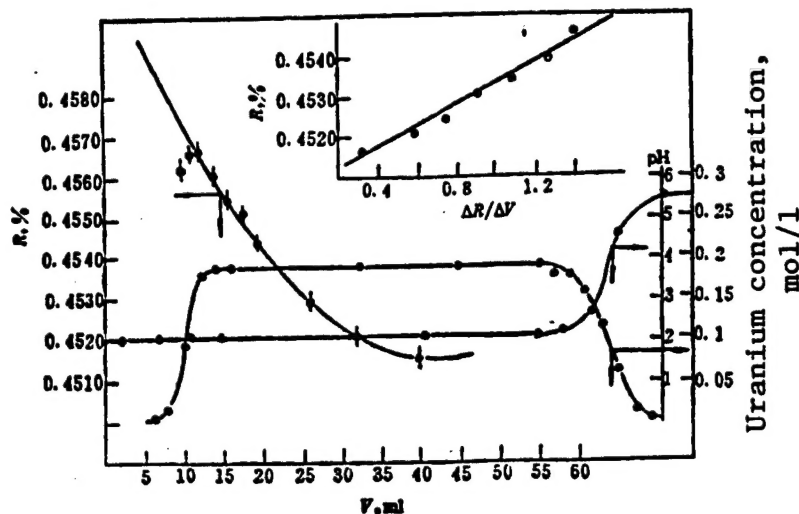**Figure 1. Experimental Results of the UO_2^{2+}-Mal-NH_4^+ Displacement System (25°C)**

From the figure we can see that ^{235}U is enriched along the leading edge of the uranium region, similar to what we often found in the literature. However, the R-V curve at the leading edge of the uranium region did not rise monotonically. Fortunately, it does not affect the computation of ε with equation (2).

From Table 2, we can confirm the following points:

1) The ε value of the UO_2^{2+}-Mal-NH_4^+ system is close to the value reported in reference 8, i.e., 2.18×10^{-4}. With the addition of succinic acid, ε declined slightly and the extent of the decrease is a function of pH*. 2) Succinic acid and

Ca^{2+} have an apparent acceleration effect on the UO_2^{2+} - UO_2^{2+} exchange. The combination could increase the value of g by 63 percent. Although ε dropped slightly, the product $\varepsilon \times g$ still went up by 37 percent. The latter is an important parameter determining the scale of the separation facility.

Since the temperature dependence of ε and g for a UO_2^{2+} - UO_2Lx exchange system has rarely been reported, uranium isotope separation was carried out at different temperatures in glass columns with the Mal-Suc-$Ca^{2+}(NH_4^+)$ displacement reagent. Figure 2 shows some typical curves. Experimental conditions and calculated results are shown in Table 3.

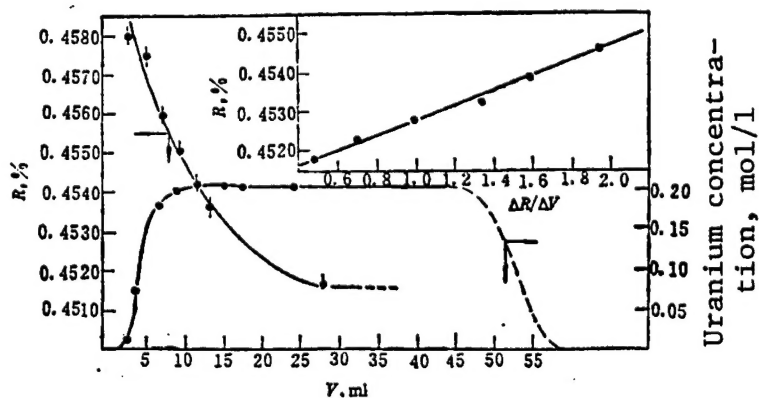**Figure 2. Experimental Results of the UO_2^{2+}-Mal-Suc-Ca^{2+} (NH_4^+) Displacement System (25°C)**

Table 3. Effect of Temperature on Uranium Isotope Separation With the $\overline{U}O_2^{2+}$-Mal-Suc-Ca^{2+}(NH$_4^+$) Displacement Reagent. Bed height 192 cm; column cross-section 0.54 cm^2; $_o$ = 0.50.

Displacement reagent concentration, mol/l	Column temperature, °C	V***, cm/min	∇, cm/min	K_d	Plateau uranium concentration, mol/l	Maximum relative enrichment[1]	$\varepsilon \times 10^4$	g, cm^{-1}
[NH$^+$] = 0.384	25	0.50	0.11	4.05	0.206	1.4%	1.94	0.50
[Mal] = [Suc] = 0.100	50	0.50	0.11	3.99	0.235	1.7%	1.86	1.15
pH** = 5.7	75	0.53	0.116	4.12	0.236	2.2%	1.77	1.27

(1) Maximum relative enrichment = [(R_{max}-R_0)/R_0] x 100%.

In agreement with the chemical exchange theory, ε drops slightly with rising temperature and g increases significantly. At 50°C, the value of ε x g is 2.2 times that at 25°C. Therefore, raising the temperature appropriately can facilitate the separation of uranium isotopes.

　　*: is p with a superimposed dot
　**: is p with a superimposed circle
***: is V with a superimposed half arrow

References

1. Qiu Ling, et al., HUAXUE XUEBAO [ACTA CHIMICA SINICA], 44, 27 (1986).

2. Jia Dongfang [6328 2639 2455], et al., GAODENGX-UEXIAO HUAXUE XUEBAO [JOURNAL OF CHEMISTRY AT HIGHER LEARNING INSTITUTIONS], 6 (12), 1045 (1985).

3. Wu Wangsuo [0702 3769 6956], et al., HE HUAXUE YU FANGSHE HUAXUE [JOURNAL OF NUCLEAR AND RADIOCHEMISTRY], 8 (3), 11 (1986).

4. Wu Wangsuo, et al., HUAXUE XUEBAO [ACTA CHIMICA SINICA], 45, 794 (1987).

5. Qiu Ling, ZHONGGUO KEXUE [SCIENCE IN CHINA], Series B, 4, 926 (1987).

6. Kakihana, H., et al., J. NUCL. SCI. TECHNOL., 14 (8), 572 (1977).

7. Kakihana, H., et al., ibid., 15 (4), 272 (1978).

8. Kim, H. Y., et al., J. CHEM. PHYS., 81 (12), Pt. II, 6266 (1984).

9. Spedding, F. H., et al., J. AM. CHEM. SOC., 77, 6125 (1985).